Plant MDL proteins synergize with the cytokine MIF on human receptors in yeast and in human immune cells

Authors: Lukas Spiller[1,2,†], Ramu Manjula[1], Franz Leissing[3], Jerome Basquin[4], Priscila Bourilhon[2,§], Dzmitry Sinitski[2,‡], Markus Brandhofer[2], Sophie Levecque[3], Simona Gerra[2], Björn Sabelleck[3], Lin Zhang[2,6], Regina Feederle[5,7], Andrew Flatley[5], Adrian Hoffmann[2,6], Ralph Panstruga[3,*], Jürgen Bernhagen[2,7,*], Elias Lolis[1,*]

Affiliations: [1]Department of Pharmacology, School of Medicine, Yale University; New Haven, CT, 06510, USA; [2]Division of Vascular Biology, Institute for Stroke and Dementia Research (ISD), Ludwig-Maximilians-Universität (LMU) München, LMU University Hospital; 81377 Munich, Germany; [3]Unit of Plant Molecular Cell Biology, Institute for Biology I, RWTH Aachen University; 52056 Aachen, Germany; [4]Departments of Structural Cell Biology and Crystallization Facility, Max-Planck-Institute for Biochemistry; 82152 Martinsried, Germany**;** [5]Monoclonal Antibody Core Facility, Helmholtz Center Munich, German Research Center for Environmental Health (GmbH); 85764 Neuherberg, Germany; [6]Department of Anesthesiology, LMU University Hospital; 81377 Munich, Germany; [7]Munich Cluster for Systems Neurology (SyNergy), 81377 Munich, Germany.

[†]Current Address: University of Ulm, Germany

[§] Current Address: Alytix Biotech, Santa Fe, Argentina

[‡] Current Address: Institute of Microbiology and Laboratory Medicine/WHO – Supranational Reference Laboratory of Tuberculosis, Martinsried, Germany

*Corresponding authors. Email: elias.lolis@yale.edu (E.L.); Juergen.Bernhagen@med.uni-muenchen.de (J.B.); panstruga@bio1.rwth-aachen.de (R.P.)

Abstract: Mammalian macrophage migration inhibitory factor (MIF) and its paralog D-dopachrome tautomerase are multifunctional proinflammatory cytokines. Plants possess orthologous MIF and D-dopachrome tautomerase–like (MDL) proteins that mimic some of the effects of MIF on immune cells in vitro. To further explore the similarities between the MDLs and MIF, we determined the structures of the three *Arabidopsis thaliana* MDLs by X-ray crystallography and tested the combinatorial effects of the plant and human proteins in functional assays. The crystal structures revealed high structural similarity between MDL and MIF homotrimers and suggested a potential explanation for lack of tautomerase activity in the MDLs. MDL1 and MDL2 interacted with each other and with MIF in vitro, in yeast, and in plant leaves and formed hetero-oligomeric complexes with MIF in vitro. The MDLs stimulated signaling through the MIF receptors CXCR2 or CXCR4 and enhanced the responses to MIF in a yeast reporter system, in human neutrophils, and in lung epithelial cells. Pharmacological inhibitors that disrupted MIF activity or prevented the formation of MIF-MDL hetero-oligomers blocked the observed synergism. These findings demonstrate that MDLs can enhance cellular responses to MIF, which may have functional implications in tissues exposed to plant proteins in the diet or environment.

INTRODUCTION

The immune defense system of vertebrates relies on a sophisticated network of innate and adaptive arms and is composed of a remarkable variety of immune cells that communicate and

traffic through a circulatory system (*1*). Cytokines and chemokines are specialized soluble immune mediators and act as coordinators of the human immune response. Accordingly, dysregulated cytokine and chemokine responses are associated with numerous diseases (*2*). Macrophage migration inhibitory factor (MIF) and its paralog D-dopachrome tautomerase (D-DT, also known as MIF-2) are multifunctional inflammatory cytokines with chemokine-like properties that are key components of the host immune response (*3-6*). MIF not only signals through its cognate receptor CD74 to control proliferation, survival, and inflammatory responses (*7*), but also engages in non-cognate interactions with the chemokine receptors CXCR2, CXCR4, and CXCR7 to promote immune cell recruitment (*8*). These activities also causally link MIF to a variety of human diseases including acute and chronic inflammatory conditions, atherosclerosis, autoimmune disorders, neurodegenerative diseases, and cancer (*4, 8-14*).

MIF- and D-DT (MIF/D-DT)–like (MDL) proteins have been identified in nearly all kingdoms of life, including uni- and multicellular parasites, fungi, and plants, suggesting that the evolutionary origin of the gene encoding an ancestral form MIF/D-DT dates back over 900 million years (*15-17*). Parasite-derived MIF orthologs can mimic mammalian MIF activities to act as virulence factors as a basis for immune evasion and are in some cases pharmacological targets (*16*). Plants have developed effective innate immune mechanisms, such as pattern recognition receptors (PRRs), to fight microbial attacks but lack an adaptive immune system (*18*). Moreover, many of the primordial organisms expressing *MIF*-like genes lack a circulation and a cell-based immune system, and in some, even the existence of G protein-coupled receptors (GPCRs), which act as secondary MIF receptors in vertebrates, is controversial. These facts have fueled speculation about MIF as an ancient enzyme that acquired extracellular functions as a cytokine in a process of neofunctionalization (*17*).

The three-dimensional structure of human MIF (*19*) bears striking resemblance to a group of bacterial enzymes consisting of 4-oxalocrotonate tautomerase (4-OT), 5-(carboxymethyl)-2-hydroxymuconate isomerase (CHMI), and malonate semialdehyde decarboxylase (MSAD) (*20*). The MIF monomer has a molecular mass of 12.5 kDa and is comprised of two α-helices tightly packed against four antiparallel oriented β-strands. However, MIF crystallizes as a homotrimer, in which three monomers interact with each other to form a barrel-shaped structure with a central solvent channel running through the protein assembly (*19*). Human MIF shares a sequence identity of < 20% with the above-mentioned microbial enzymes, but has a tautomerase catalytic cavity between its subunits and an unusually acidic N-terminal proline residue, exposed after proteolytic removal of the initial methionine residue, with a pKa of 5.6, consistent with a function as a catalytic base (*21*-*23*). Although MIF can catalyze the tautomerization of the non-physiological substrate D-dopachrome (or D-dopachrome methyl ester [DME]) and enol-keto forms of the physiological molecule 4-hydroxyphenylpyruvate (HPP) in vitro (*21, 22*), a bona fide substrate for MIF activity in humans has remained elusive, and a role for the enzymatic activity in human cells has not been clearly demonstrated. However, mutational and inhibitor studies have demonstrated that changes in the catalytic cavity lead to conformational alterations that affect MIF binding to CD74, CXCR2, and CXCR4 (*24*-*28*). The tautomerase catalytic site has been used in a variety of methods to identify small molecule inhibitors that affect several mouse models of disease. Although much less studied, MIF also features redox-regulatory activity related to its redox-sensitive cysteine residues (*29*) and has been suggested to have nuclease activity owing to a PD-D/E(X)K nuclease motif (*30*).

Comparison of MIF and MDL proteins across different kingdoms reveals a high degree of sequence conservation, with many sites being under selection in some kingdoms, especially in

plants (*17, 31*). Conservation is high for the tautomerase site, whereas other motifs known to be of functional importance in human MIF, such as (the pseudo-*E*LR motif required for CXCR2 binding) are not well conserved (*32*). There seems to be a complex interplay between vertebrate MIF and parasite MIF orthologs, with implications for virulence and host defense (*33*).

Regarding MDLs in the plant kingdom, in silico analysis has demonstrated an extraordinary degree of evolutionary conservation in these proteins and the genes that encode them, and they may have a role in development and defense (*17, 34*). Multiple *MDL* genes are typically present per plant species, including model plants such as *Arabidopsis thaliana*, as well as crops and other food plants. The three *Arabidopsis* MDLs (*At*MDLs; herein termed MDLs for simplicity) share a sequence identity of 28–33% with human MIF, with higher conservation in the tautomerase cavity (fig. S1) (*35*). MDL1 and MDL2 localize to the cytoplasm of plant cells, whereas MDL3 resides in peroxisomes (*34*). In vitro assays indicate that the tautomerase activity of MDLs for the artificial substrates HPP and D-dopachrome is greatly reduced in comparison to human MIF (*36*). Given the sequence homology between MDLs and human MIF, we previously tested whether MDLs would interact with components of the human MIF signaling network, similar to the virulence paradigm established for parasite MIF orthologs (*16, 33, 37*). We observed an unexpected degree of cross-kingdom mimicry, with MDLs binding to and activating the human MIF receptors CXCR4 and CD74 and promoting the chemotaxis of human leukocytes (*36*). This observation expanded the previously established interplay between the plant immune system and MIF proteins delivered by the plant-parasitic aphid *Acrythosiphon pisum*, suggesting the possibility of an unanticipated cross-kingdom interaction between components of the plant and human immune system (*38*).

In this study, we sought to characterize the structures of MDLs and understand the mechanisms underlying the interplay between plant MDLs, human MIF (hereafter referred to as MIF), and MIF receptors. We determined the crystallographic structures of all three *Arabidopsis* MDLs, identified structural similarities between MDLs and MIF, and unraveled the presumed basis for the unexpectedly low tautomerase activity of MDLs. We demonstrated by biochemical, cell biological, and biophysical methodologies that MDLs and MIF formed hetero-oligomeric complexes that affected MIF-driven receptor responses by cross-kingdom synergy.

RESULTS

Crystal structures of *Arabidopsis* MDLs reveal high structural similarity to human MIF and a putative basis for their lack of tautomerase activity

We expressed and purified recombinant C-terminally hexahistidine-tagged MIF orthologs MDL1-6×His, MDL2-6×His, and MDL3-6×His (thereafter referred to as MDL1, MDL2, and MDL3) (fig. S2, A to C). The X-ray structure of these three MDLs was solved and refined to 1.56 Å, 1.40 Å, and 2.00 Å resolution, respectively (Fig. 1A; table S1). All three MDL proteins crystallized as trimers with a very high overall structural similarity to the human MIF trimer, including three 3_{10}-helices (Fig. 1A) with a root mean square deviation (RMSD) ranging from 0.734 Å for MDL1 to 0.906 Å for MDL3 (Fig. 1B). Analysis of a structure-based alignment revealed 27% sequence identity for an all-against-all comparison of all three MDLs and 12% sequence identity for a comparison of the three MDLs with MIF (fig. S1) (*35*). The 14 invariant residues per monomer in the structural alignment (fig. S1) are localized into separate regions:

region 1 is the catalytic cavity between two subunits and contains Pro^{1} and Ser^{63} (all residue numbering refers to that for MIF; fig. S1), whereas region 2 is a discontinuous surface outside the catalytic cavity composed of the six residues Ala^{27}, Gly^{31}, Pro^{33}, Gly^{65}, Ser^{63}, and Asp^{100} (fig. S3, A and B). In region 3, a major portion of the Asp^{100} surface area is outside the solvent channel, adjacent to the MIF allosteric site residue Tyr^{99}, the side chain of which is within the channel serving as a solvent gating residue (fig. S3C) (*26*). MDL1 and MDL2 also have a tyrosine residue at the equivalent position, and MDL3 has a phenylalanine residue (fig. S1). Of note, there are three residues that belong to multiple regions based on their structural orientation. For example, Ser^{63} is part of both regions 1 and 2 with the hydroxyl group being part of the catalytic cavity and its backbone contributing to the surface area (fig. S3B). Asp^{100} belongs to region 2, where Gly^{65} makes a hydrogen bond between their backbone atoms, but the side chain of Asp^{100} is the only residue in region 3. At region 4, the Arg^{93} side chain makes a hydrogen bond to the backbone of Phe^{49}, which is at the C-terminal end of a β-strand involved in subunit-subunit interactions and serves a role in stabilizing this β-strand that provides the specificity for MDLs and MIF to form homotrimers (fig. S3D). Regarding the remaining seven invariant residues, (Thr^{7}, Asn^{8}, Phe^{49}, Gly^{51}, Ala^{57}, Leu^{83}, and Arg^{93}) with Ala^{57} and Leu^{83} are buried within the hydrophobic core of the protein, and Thr^{7}, Asn^{8}, Phe49, Gly^{51}, and Arg^{93} are localized in loop regions (fig. S3A).

We also examined the tautomerase catalytic cavity in more detail, focusing only on the structures of the MDLs. The electrostatic potential of the catalytic cavity of MDL3 was low, consistent with a lack of catalytic activity for HPP. A view of the electrostatic potential of MDL1 and MDL2 did not explain the large difference in catalytic activity between MIF and MDL1 or MDL2, because each displayed high active site identity and a positive electrostatic potential at

the active site (Fig. 1A). We therefore superimposed each MDL on the MIF-HPP enzyme-substrate complex to create a model of HPP interacting with the MDLs' catalytic sites (Fig. 1B) (*39*). The interactions were analyzed and compared to the respective MIF-HPP complex. The major difference in catalytic residues between human MIF (Pro^{1A}, Lys^{32A}, Ser^{63A}, Ile^{64A}, Tyr^{95C}, and Asn^{97C}, where A, B, and C refer to the trimer subunits) and those of the three MDLs was Lys^{98C}. Note that MDL Lys^{98} is equivalent to MIF Asn^{97} due to an extra residue in the alignment (fig. S1). Substitution of Asn^{97} in MIF by lysine markedly reduces the tautomerase activity for both HPP and DME (*36*), suggesting that Asn^{97} in MIF is important for the tautomerase enzymatic activity of MIF using these artificial substrates, whereas a lysine residue in this position in MIF would not support the enzymatic activity. In turn, this may imply that the lysine residue at that position in the MDLs (Lys^{98}) may not support or may even obstruct the enzymatic tautomerase activity. In fact, when we inspected the position of this residue in detail, the major structural difference between MDL1 and MIF was the different side chain orientation of Lys^{98}, which was oriented away from HPP with a distance >5.4 Å for all three subunits in MDL1. By contrast, the side chain amide group of Asn^{97} in MIF formed a hydrogen bond with HPP (Fig. 1C). The large distance between Lys^{98} of the MDLs and HPP was similar in the analysis for MDL2 and MDL3 with the modelled HPP, resulting in a loss of a hydrogen bond interaction and apparent decreased affinity for HPP (fig. S4, A and B).

An unanticipated difference was observed in MDLs at residue 96, which is the equivalent position of MIF Tyr^{95} (fig. S1). The side chain of Tyr^{96} for MDL1 had different conformations in the three subunits. In one subunit it clashed with the modelled HPP, and in the other two subunits the side chain had no predicted interactions with HPP. The equivalent residues for MDL2 and MDL3 are Phe^{96} and Ile^{96}, respectively. The proteins differed in the position of these residues

from Tyr^{96} in MDL1, with Phe^{96} of MDL2 making van der Waals interactions with HPP (fig. S4A), while the Ile^{96} of MLD3 was not predicted to interact with HPP at all (fig. S4B). Together, the crystal structures of *Arabidopsis* MDLs revealed a high overall structural similarity to human MIF. This similarity was even more striking at the catalytic cavity with exceptions at residues Lys^{98} (which replaces Asn^{97} in MIF) and Tyr^{96}, Phe^{96}, Ile^{96} (which replace Tyr^{95} in MIF). A different orientation and conformation of these residues, respectively, could be the basis of the inactive tautomerase catalytic site in the Arabidopsis orthologs.

MIF and MDLs engage in direct protein-protein interactions in vitro, in cells, and in planta

The high degree of structural similarity between MIF and the three MDLs and the capacity of each of these proteins to form homotrimers prompted us to investigate whether these proteins would also physically interact with each other across kingdom boundaries. To test this possibility experimentally, we first performed in vitro coimmunoprecipitation assays with MIF and MDL1 as a representative of the three MDLs. Purified MDL1-6×His and biotinylated MIF-6×His were mixed, complexes pulled down by streptavidin-coated magnetic beads, and the resulting eluate analyzed by blotting and detection with horseradish peroxidase–conjugated streptavidin to verify precipitation of biotinylated MIF-6xHis and with the custom-made, MDL1-specific monoclonal antibody Atm1 21G9 (fig. S5) to detect coprecipitated MDL1-6×His (Fig. 2A). Complex formation was further confirmed by analyzing immunoblots with an antibody specific for the histidine tag (fig. S6). This revealed an association of the recombinant MIF and MDL1 proteins in vitro.

To determine whether interactions between MIF and MDL also occurred in cells, we tested all pairwise interactions between MIF, MDL1, MDL2 and MDL3 in yeast-two-hybrid assays.

Similar to our previous report (*34*), we detected a weak homomeric MDL1-MDL1 interaction and a strong heteromeric MDL1-MDL2 interaction in this system. In accordance with earlier biochemical evidence (*19, 40, 41*), we also noticed a homomeric MIF-MIF interaction. MIF-MDL2 complex formation occurred in yeast, when MDL2 was used as the bait protein (Fig. 2B), but not when MIF was used as bait. To substantiate these findings suggesting direct binding between human MIF and a plant MDL, we performed in planta luciferase complementation imaging (LCI) assays. In this experimental setup, fusion proteins tagged with enzymatically inactive N- and C-terminal segments of firefly luciferase (nLUC and cLUC, respectively) were transiently expressed in *Nicotiana benthamiana* leaves (fig. S7A). Interaction of candidate proteins led to the reconstitution of enzymatically active luciferase, which was detected and quantified upon addition of the substrate luciferin. Co-expression of nLUC-MIF with cLUC-tagged MDL1, MDL2, MDL3 or MIF resulted in strong luciferase activity for the cLUC-MDL2 and nLUC-MIF combination. Similarly, expression of cLUC-MIF yielded strong luciferase activity in the reciprocal combination with nLUC-MDL2 and additionally with nLUC-MIF (Fig. 2, C and D; fig. S7B). To quantify direct binding between MIF and its MDL homologues, we determined the K_D values of MIF-MDL interactions using microscale thermophoresis (MST), a biomolecular interaction methodology suitable to measure protein-protein binding at nano- to micromolar concentrations under solution conditions. We chemically labeled recombinant MIF with the RED-NHS dye to analyze the interaction with unlabeled recombinant MDL1, MDL2, and MDL3, respectively. We observed characteristic sigmoidal binding curves with K_D values less than 5 µM for each MIF-MDL pair (Fig. 2E). Several negative controls, including buffer (fig. S8A), BSA (fig. S8B), and heat-denatured MDL1 protein (fig. S8C) did not result in sigmoidal binding curves, indicating the MIF-MDL interactions were due to specific binding.

Taken together, four different types of protein-protein interaction assays (in vitro coimmunoprecipitation, yeast two-hybrid, in planta LCI experiments, and in vitro MST) provided evidence for direct association of MIF and MDL proteins.

MIF and MDLs synergistically activate human chemokine receptors in yeast

We have previously used a genetically modified strain of *Saccharomyces cerevisiae* that expresses functional human chemokine receptors that signal through an altered *S. cerevisiae* Gα (GPA1) protein. In this system, GPA1 activation stimulates the mitogen-activated protein kinase (MAPK) pathway, the transcription factor STE12, and STE12-dependent expression of a β-galactosidase (*lacZ/ß-gal*) reporter (*25*, *42-45*) (Fig. 3A). Capitalizing on this established system for assaying CXCR4 activation (*25*) and an analogous yeast strain expressing CXCR2 generated herein, we tested MIF and the MDLs for activation of intracellular signaling downstream of CXCR4 and CXCR2.Due to its subcellular localization, we focused in these studies on MDL1 and MDL2. Both MDL1 and MDL2 activated CXCR4 more potently than did MIF, with each protein used at 20 µM (Fig. 3B). When 10 µM MIF with 10 µM of either MDL1 or MDL2 were tested together, a hyper-activated (synergistic) effect was observed with the MIF-MDL2 mixture approximately three times more active than the MIF-MDL1 combination (Fig. 3B). We also verified the specificity of the synergistic effect applying an otherwise isogenic yeast strain lacking CXCR4, which was generated by a plasmid loss approach from the CXCR4-expressing strain (*46*). This experiment confirmed that only negligible reporter activity was measurable in the absence of CXCR4, thus essentially excluding effects by endogenous yeast factors (fig. S9, A and B). Activation of the chemokine receptor CXCR2 by MIF occurs in mammalian cells (*8*, *28*, *32*). The MDLs lack the pseudo-*E*LR motif of two non-adjacent residues present in human MIF

(Arg^{11} and Asp^{44}) that contributes to binding and activation of CXCR2 (*32*). Consequently, MDL1 and MDL2 were not expected to activate CXCR2. However, application of 20 µM MIF, MDL1, and MDL2 revealed that MDL1 and MDL2 activated CXCR2 to a greater extent than did MIF, even though the MDL proteins contain uncharged residues in positions 11 and 44 (Fig. 3C, fig. S1). Given the results with CXCR4, we also tested whether the co-application of MIF and MDLs affected activation in the CXCR2-dependent yeast reporter system. Similar to the effect seen for CXCR4, joint application of MIF with either MDL1 or MDL2 resulted in hyperactivation, indicating a synergistic effect on CXCR2 activation when MIF was mixed with either MDL1 or MDL2 (Fig. 3C).

We used pharmacological probes to support these results. The MIF small molecule inhibitor 4,5-dihydro-3-(4-hydroxyphenyl)-5-isoxazoleacetic acid methyl ester (ISO-1) binds to the tauto-merase pocket of MIF, thereby inhibiting its catalytic activity as well as its CD74-mediated induction of MAPK activation, p53-dependent apoptosis, and cell proliferation (*47-49*). ISO-1 was previously also shown to partially block MIF-CXCR4 reporter activation (*42*) and MDL1-induced monocyte chemotaxis (*36*), indicating that this inhibitor might likewise affect CXCR4 activation by MDL1. In the yeast-based CXCR4 reporter system, co-application of ISO-1 (100 µM) with MIF, MDL1, or MDL2 strongly reduced the activating capacity of these proteins (Fig. 3D). We also noticed a marked reduction of the synergistic effect triggered by the joint application of MIF with MDL1 or MDL2 by ISO-1. The FDA-approved drug AMD3100 is a CXCR4 receptor antagonist that prevents the binding of CXCR4 ligands such as CXCL12, and partially inhibits MIF, thus constraining CXCR4 signaling (*25*). Using AMD3100 in the yeast reporter assay at a 10-fold molar excess over the concentration of the tested ligands, we observed significantly reduced CXCR4 activation by MIF and MDL2, both in single application and in

combination of the two proteins (Fig. 3E). For MDL1 alone there was no inhibition by AMD3100 and only a mild reduction in signaling when co-applied with MIF. The CXCR2 antagonist SB225002 (*50*) (used at 20-fold molar excess over the ligands) reduced activation by MIF, MDL1, and MDL2 to similar degrees (Fig. 3F).

To further explore the observed synergistic effect between MIF and the MDLs, we performed concentration-response experiments, using the synergism between MIF and MDL1 on CXCR4 (Fig. 3B) as an example. We initially co-incubated the previously applied concentration of 20 µM MIF with 1-4 µM of MDL1. Synergy occurred at 1 µM MDL1 and further increased at higher concentrations, with a 5-fold enhancement of reporter activity at 4 µM MDL1 (Fig. 3G). To study synergy in greater detail, we next used a sub-threshold concentration of 1 µM MIF while varying MDL1 from 0.01 to 10 µM. A significant synergistic effect was already noted at 1 µM MDL1 and continuously increased at higher concentrations (Fig. 3H). The apparent EC_{50} for a synergistic effect of MDL1 under 1 µM MIF for this assay was determined to be 2.5 - 3 µM (Fig. 3, H and I; fig. S10, A-D). A similar value was determined when the luminescence response of the MDL1-alone treatment was subtracted (fig. S11, A-D) (*51*). Together, the results of these experiments showed MDL1 and MDL2 were better agonists than MIF when used alone. When used in combination with MIF, MDL1 or MDL2 induced receptor hyperactivation, which was largely blocked by MIF-, CXCR2-, or CXCR4-specific small molecule inhibitors.

MIF-MDL hetero-oligomers are responsible for synergism

MIF can form various stable types of trimers or homo-oligomers, whereas monomers and dimers are less stable (*24, 40, 52-54*). This prompted us to investigate if MIF and MDLs can also form hetero-oligomers, which could be the basis of the observed synergistic effect on CXCR2 and

CXCR4 receptor activation. MIF and MDL1 each eluted as trimers when individually subjected to size exclusion chromatography (SEC) (Fig. 4A), but a mixture of MIF and MDL1 showed formation of potential hexamers in addition to trimers (Fig. 4B). Elution volumes and protein markers were used to obtain a calibration curve (fig. S12, A and B) and to derive a standard equation (fig. S12C) to accurately calculate molecular masses from observed elution volumes (fig. S12D). This allowed estimations for the molecular masses of MIF (43.8 ± 0.7 kDa) and MDL1 (38.0 ± 0.3 kDa), as well as MDL2 (35.9 ± 0.6 kDa), when the proteins were applied individually (Table 1). These masses are well in line with the expected masses of the respective trimers. The estimated molecular masses obtained for SEC analysis of the MIF and MDL1 mixture were determined to be 38.5 ± 0.7 kDa and 82.5 ± 0.6 kDa (Table 1), values that are in good agreement with the molecular masses of a (homo- or heteromeric) trimer and a hetero-oligomeric hexamer, respectively.

We noticed that only approximately one third of the MIF and MDL1 mixture formed hetero-hexamers (Fig. 4B). To establish whether this proportion of the hetero-hexamer had any functional role, we used the molecule p425, a sulfonated azo compound and allosteric MIF inhibitor proposed to bind at the interface of two adjacent MIF trimers (Fig. 4C) and to inhibit MIF tautomerase and CD74 activities (*52*, *53*). We tested whether p425 affected hetero-hexamer formation between MIF and MDLs using SEC and MST assays. In the presence of 100 µM p425, binding of MIF to MDL1 was disrupted, as indicated by a disappearance of the putative hexamer peak in the SEC chromatogram (Fig. 4D). Furthermore, no direct binding was observed in the MST experiment with the MIF-p425-MDL1 mixture (Fig. 4E) or for the MIF-p425-MDL2 and MIF-p425-MDL3 mixtures (fig. S13, A and B).

To investigate whether the trimer or hexamer contributed to the observed activation and synergism in the yeast-based assay, we used p425 (100 μM) in the CXCR4 signaling assay with application of the individual agonists MIF, MDL1, or MDL2 alone, or with co-application of MIF with MDL1 or MDL2. Signaling activity was completely abolished by p425 with the individual proteins (Fig. 4F), suggesting that activation of CXCR4 requires access to the tautomerase site, in agreement with our findings with the MIF small molecule inhibitor ISO-1 in the yeast-based CXCR4 reporter system (Fig. 3D) and in mammalian cells (*25*). Co-administration of p425 with MIF and either MDL1 or MDL2 also significantly reduced CXCR4 synergistic activity to slightly above basal amounts (Fig. 4E). This result, together with the SEC and MST data, strongly suggested that the observed synergism was due to a hexamer formed by trimeric MIF and a trimeric MDL.

MIF and MDL1 synergistically promote chemotactic migration of human neutrophils

To determine whether synergism occurs in human cells, we tested the effect of MIF and MDL1 on primary human neutrophil chemotaxis, because neutrophils abundantly produce CXCR2 and CXCR4 (but not CD74), and have been shown to migrate upon stimulation with MIF (*50*). Neutrophil chemotaxis was first examined in a Transwell migration device (fig. S14A). MDL1 was added to the lower chamber as chemoattractant and its chemotactic activity towards neutrophils in the upper chamber compared with MIF and 10 ng/mL CXCL8 as a bona fide CXCR2 agonist and positive control. MDL1 increased neutrophil chemotaxis in a concentration-dependent manner, with a typical bell-shaped curve and a maximal chemotactic index of approximately 2 observed at 500 ng/mL. This effect was significantly higher than that of 500 ng/mL MIF (Fig. 5A). Of note, experiments comparing chemotaxis of a mixture of 250 ng/mL

MIF and 250 ng/mL MDL1 versus chemotaxis by an individual regimen of 500 ng/mL MIF or 500 ng/mL MDL1 demonstrated synergism (Fig. 5B).

We next studied 3D-chemotaxis of primary human neutrophils as assessed by single-cell migration tracks in the x-y direction using live-cell microscopy (fig. S14B). As expected, compared to the negative control (buffer), the positive controls 500 ng/mL CXCL8 and 500 ng/mL MIF led to a significant shift in migration tracks from a random distribution to chemotaxis towards the chemokines (Fig. 5, C to E; fig. S15, A to C; fig. S15F). MDL1 had a similar pro-migratory effect as MIF (Fig. 5F; fig. S15, D and F). Again, addition of a MIF and MDL1 mixture produced a synergistic effect (Fig. 5, G and H; fig. S15, E and F).

We next tested the effect of the CXCR2 and CXCR4 inhibitors SB-225002 and AMD3100, respectively, on MIF- or MDL1-induced neutrophil chemotaxis in both Transwell and 3D-live imaging chemotaxis assays. When assessed by Transwell assay, MIF-induced neutrophil chemotaxis was inhibited by both the CXCR2 and CXCR4 antagonists, but MDL1-induced chemotaxis was only inhibited by SB-225002 across the entire concentration range from 100 to 1000 ng/mL (Fig. 6A). The difference in inhibitor effects between MIF and MDL1 might be explained by only partially overlapping receptor binding sites. Similar results were observed with 3D chemotaxis viewed by live-cell microscopy. The CXCR4 antagonist AMD3100 only inhibited MIF-induced chemotaxis, but not that elicited by MDL1 (Fig. 6, B; fig. S16, A and C), whereas the CXCR2 antagonist SB-225002 inhibited chemotaxis induced by both proteins (Fig. 6, C; fig. S16, B and C). In summary, these results were quantitated in Fig. 6D and were similar to those obtained with the *S. cerevisiae* signaling system (Fig. 3, E and F), overall indicating that MDLs can elicit MIF chemokine receptor-mediated responses and interact synergistically with MIF in human cells.

MIF and MDL1 synergistically promote AKT signaling downstream of CXCR4 and inflammatory gene expression in human lung epithelial cells

To test MIF receptor activation by MDLs and their synergistic effects with MIF on another human cell type, we assessed the effects of MDLs individually and in combination with MIF on the A549 human lung epithelial cell line. This cell line is a well-established model for human type II pneumocytes that has been used for a variety of studies on lung inflammation and infection (*55*), and MIF is known to promote inflammatory effects in pneumocytes (*12*). Flow cytometric analysis of known MIF receptors showed this cell line to produce substantial amounts of CXCR4, whereas CXCR2, CXCR7, and CD74 were not detected in our analysis (fig. S17A). MIF can bind and activate CXCR4 to elicit downstream activation of phosphoinositide 3-kinase (PI3K) and the kinase AKT that is relevant in both physiology and pathophysiology (fig. S17B) (*56*). In line with previous studies, we observed an increase in phosphorylated AKT (pAKT) abundance up to 3-4-fold within 15 min of MIF stimulation (Fig. 7, A and B) (*57*, *58*). We also confirmed the previously described capacity of MDL1 to activate AKT signaling (Fig. 7, A and B) (*36*). Of note, an equimolar co-application of MIF and MDL1 resulted in a markedly stronger effect with an increase in pAKT concentrations of 8-9-fold (Fig. 7B). Taken together, these data supported a synergistic mechanism for AKT signaling promoted by MIF and MDL1 in A549 lung epithelial cells.

Lung macrophages and lung epithelial cells are important sources of inflammatory mediators following the inhalation of potentially harmful material. We therefore also used RT-qPCR to measure the expression of major proinflammatory mediator genes *TNF-α*, *IFN-γ*, *CCL2*, *IL1-β*, *IL-6*, and *CXCL8* in A549 cells after stimulation with bacterial lipopolysaccharide (LPS), MIF,

MDL1, or a combination of MIF and MDL1 (Fig. 7, C to H). LPS stimulation resulted in a very strong (10-120-fold) increase in inflammatory gene expression in A549 cells for all cytokine genes examined, with strongest effects observed for *IFN-γ* and *TNF-α*. MIF increased the expression of all tested proinflammatory genes, although to a lesser degree than did LPS. The strongest MIF effects were seen for *TNF-α* and *IL-6*, which increased over baseline by about 6-fold (Fig. 7, C to H). Stimulation by MDL1 activated proinflammatory cytokine gene expression in a range similar to that observed for MIF, with slightly stronger increases for all transcripts (Fig. 7, C to H). When A549 cells were stimulated with a combination of MDL1 and MIF, inflammatory cytokine gene induction was significantly stronger than for treatment with either alone, showing an observed rate of increase of 5-40-fold. This synergistic effect was most pronounced for *IFN-γ*, *TNF-α,* and *IL-6* (Fig. 7, C to H). Together, these data demonstrated that MDL1 stimulated AKT activation in CXCR4-expressing human lung epithelial cells and induced proinflammatory cytokine responses. They also showed a marked synergistic effect for the combination of the human MIF and plant MDL1 proteins that was particularly pronounced for the cytokine gene expression response. These results are consistent with MDL1 promoting intracellular signaling and proinflammatory gene expression in lung epithelial cells by binding to CXCR4 and show that MDL1 can enhance the responses of lung epithelial cells to MIF. Overall, our findings demonstrate that MDLs bound and activated CXCR4, stimulated CXCR4-dependent migration of primary human neutrophils, and elicited cellular proinflammatory responses in cultured human lung epithelial cells similarly to MIF. MDLs formed hetero-oligomeric complexes with MIF in vitro and synergistically promoted MIF responses in cells.

DISCUSSION

We investigated structural, biochemical, and functional properties of MDLs, plant orthologs of the atypical human cytokine MIF. Analysis of the structural data obtained for all three *Arabidopsis* MDLs showed an extraordinary degree of structural conservation with the overall architecture of mammalian MIF proteins, including the enzymatic site, thereby confirming previous sequence-based in silico modelling (*31*). Despite the high degree of conservation at the tautomerase active site, a striking difference in enzymatic catalysis was previously observed for all three MDLs in comparison to MIF (*36*). The crystal structures in our present study may offer a structural explanation for this observation. Lys^{98}, which is present in all three MDLs and replaces Asn^{97} in MIF, has no stabilizing interaction with the modelled substrate, HPP. In addition, there are other residues that differ between the MDLs and MIF, such as Tyr^{96} of MDL1, which has a different conformation than the corresponding tyrosine in MIF (Tyr^{95}), and the existence of Phe^{96} and Ile^{96} at this position in MDL2 and MDL3, respectively. A different orientation or conformation of these residues in the three-dimensional context of the cavity could be the structural basis of the inactive tautomerase catalytic site in the *Arabidopsis* orthologs (*36*). However, we cannot eliminate the possibility that binding of HPP to the MDL1 or MDL2 enzymatic site occurs in a non-productive manner for catalysis, because the MIF inhibitor ISO-1 was designed based on the MIF-HPP structure (*39*) and inhibits MDL-mediated activities.

We present evidence for direct protein-protein interaction and cooperative signaling of MIF with MDLs tested in a variety of systems, including yeast two-hybrid assays, in planta experiments, MST, CXCR2 and CXCR4 signaling assays, and inhibition of signaling by pharmacological

agents affecting MIF, CXCR2, and CXCR4 as well as MIF-MDL oligomerization. Furthermore, we obtained evidence for synergistic effects of MDL1 and MIF on inflammatory responses of human cells that can also be explained by protein-protein interactions or cooperative signaling. We acknowledge that some assays revealed an MIF-MDL2 interaction, while none was seen for MIF-MDL1. For example, in the yeast two-hybrid and in planta luciferase complementation assays, we found that only MDL2 interacted with MIF. By contrast, both MDL1 and MDL2 interacted with CXCR2 and CXCR4 in the yeast signaling system, and SEC showed interactions between MIF and MDL1 that were abrogated by the inhibitor p425. Further studies are necessary to provide an explanation for the observed MDL paralogue–specific differences depending on the assay. Moreover, we detected homomeric MDL1-MDL1 and heteromeric MDL1-MDL2 interactions in the yeast two-hybrid assay, confirming a previous in planta analysis (34). The assay does not provide any information as to whether these represented interactions of MDL subunits within a trimer or allosteric interactions between MDL trimers. To this end, future studies will be needed to clarify if and to what extent homomeric MDL or MIF oligomerization competes with MDL-MIF hetero-oligomerization.

Plant cells do secrete proteins, but there is no evidence that MDLs are exported outside the cell (*34*). Furthermore, there are no proteins resembling the MIF receptors for MDLs to activate these types of receptors in plants. Although the absence of proteins resembling known receptors does not exclude the possibility that MDLs activate other receptors or intracellular proteins, evidence points to MDLs functioning as intracellular cytoplasmic (MDL1 and MDL2) or peroxisomal (MDL3) enzymes. To understand the role of MDLs in plant life, the respective physiological substrate needs to be identified for each MDL.

Whereas the yeast, in planta, and MST assays did not yield stoichiometric information, the SEC experiment suggested that a dimer of two different MIF-MDL homotrimers was formed and was functionally active. This conclusion was supported by experiments using the inhibitor p425, which prevented or disrupted oligomerization as analyzed by SEC, blocked MIF-MDL1 binding in the MST assay, and attenuated hetero-oligomer–mediated synergism in the CXCR2- or CXCR4-engineered strains of *S. cerevisiae*. Its mode of action involves intercalation between the interface region of two MIF trimers, thereby inhibiting MIF-mediated inflammatory responses (*52*, *53*, *59*). We would eliminate the possibility that there is a mixture of MIF and MDL within a trimer due to the dissociation rate of 7.7×10^{-16} M^2 for MIF as determined by sedimentation velocity and equilibrium experiments (*54*). Although the dissociation rates of the MDLs have not been measured, we assume, in analogy to MIF, they function as tight trimers and that the MDL1-MDL2 association observed in the two-hybrid assay was also based on an oligomer of homo-trimers, which also might be important information for determining the functional role of MDL1-MDL2 complexes in plants.

Given the results of the protein-protein interaction experiments, we probed whether there was signaling activity in a genetically modified strain of *S. cerevisiae* expressing functionally active CXCR4 (*25*, *42-45*). In addition to CXCR4, in the present study CXCR2 was also used for analogous experiments. Both MDL1 and MDL2 induced signaling through CXCR2 and CXCR4. The MIF inhibitor ISO-1 inhibited CXCR4 signaling by both MDLs, but antagonists of CXCR2 (SB-225002) and CXCR4 (AMD3100) had different effects on MDL1- and MDL2-mediated signaling. Whereas SB-225002 and AMD3100 inhibited MDL2-mediated activation of CXCR2 and CXCR4, respectively, there was significantly reduced or no effect of AMD3100 on CXCR4 activation by MDL1, suggesting an allosteric mechanism of MDL1 activation that bypasses the

CXCR4 transmembrane cavity that is necessary for orthosteric activation (*60*). This finding thus also illustrated the plasticity of CXCR4 activation and must play a role in the synergy that occurred when MDL1 or MDL2 were mixed with MIF to costimulate either CXCR2 or CXCR4. The inhibitors (ISO-1, SB-225002, and AMD3100) decreased activation of the receptors. To assess how these two MIF-MDL complexes synergized, the inhibitor p425, which greatly reduced synergism to almost basal amounts, provided initial insight. To gain greater mechanistic insight as to whether MIF and MDL1 and MDL2 associated or acted independently to achieve signaling synergy, we used SEC to show that MIF and MDLs combined to form a putative trimer-trimer (hexameric) complex.

The synergism between MIF and *Arabidopsis* MDLs that occurred in vitro and in *S. cerevisiae* genetically modified to express functional chemokine receptors are not physiological. To investigate whether these interactions have biological relevance, we considered mammalian tissues and organs that could potentially interact with plants or plant cells, with the most obvious being the integumentary, digestive, and pulmonary systems. We chose to examine synergism between human MIF and plant MLDs using primary human neutrophils and the human lung epithelial cell line A549. We studied neutrophil chemotaxis, AKT activation, and proinflammatory gene expression as functional readouts of the host immune and inflammatory response. Of note, we found that synergistic MIF-MDL1 effects shaped both neutrophil migration and the inflammatory response of A549 cells. The receptor antagonist and receptor expression profiles suggested that synergism in neutrophils involved both CXCR2 and CXCR4, whereas the synergistic effects in A549 cells were likely mediated by CXCR4.

Despite the synergism we observed, we realize the cross-kingdom interactions between human MIF and *Arabidopsis* MDLs, which share high sequence identity with MDLs from other plants,

are unexpected. We speculate mammalian MIF activity might be affected by direct association with plant-derived MDL proteins following contact with skin, inhalation of plant particles or smell, or upon initiating food ingestion in the pharyngeal tract or gut. For example, interactions might occur with immune cells within pharyngeal secondary lymphoid organs or with intestinal MIF by MDL fractions that have escaped digestion (*61*) . It could be further speculated that synergism with host proteins could potentially be involved in hyperactivation responses of the integumentary or digestive system, but this aspect has not been explored. In addition, other plant extracts are identified as "medicinal plants" with immunomodulatory activities on mammals through mechanisms that remain poorly understood. Plant-derived peptides (*62*) and proteins (*63*) have been likewise proposed to affect mammalian immune status and may be involved in enhancing allergic or inflammatory mechanisms. Although *Arabidopsis* is neither a "medicinal" nor an "edible" plant, the highly sequence-related MDL orthologs are omnipresent in other species of the plant kingdom (*31*). Additional in vitro and in vivo studies are necessary to test the hypothesis that the activity of MIF proteins as components of the human system might be altered when exposed to plant MDL proteins. Such studies involving MIF and MDLs are needed to broaden our understanding of these proteins in potential cross-kingdom interactions.

MATERIALS and METHODS

Expression and purification of recombinant proteins

Clones of MIF and the three *A. thaliana* MIF ortholog genes, *MDL1*, *MDL2*, and *MDL3* in pET21a were previously generated (*64*) and used in this work. Briefly, classical cloning

strategies were applied, and all genes were C-terminally fused to a hexahistidine tag included in the pET21a vector using the restriction endonucleases *Nde* I and *Xho* I. Plasmids were transformed into competent *Escherichia coli* RosettaTM (DE3) cells to express the pET21-derived genes and to yield MIF–6xHis, MDL1–6×His, MDL2– 6×His, and MDL3–6×His fusion proteins. Protein expression was induced by isopropyl-β-D-thiogalactopyranoside (IPTG; Sigma, Deisenhofen, Germany)) as previously described (*36*).

To release intracellular protein, a high-pressure cell homogenizer (French press, Avestin EmulsiFlex C5 by Avestin Europe GmbH, Mannheim, Germany) was used to lyse cells at approximately 75 MPa. Homogenization as well as all following purification steps were carried out on ice and under constant cooling. For homogenization, fresh or frozen bacterial pellets gently thawed on ice were resuspended in 1 mL ice-cold immobilized metal affinity chromatography (IMAC) binding buffer (20 mM sodium phosphate, 0.5 M NaCl, 20 mM imidazole, pH 7.2). Lysates were then centrifuged at 18.000 × *g* for 30 min at 4 ºC to remove cell debris. The protein-containing supernatants were collected and filtered prior to usage in fast protein liquid chromatography (FPLC; ÄKTA Pure, GE Healthcare/Cytiva, Freiburg, Germany).

For purification, IMAC and subsequent SEC were performed on an FPLC. Nickel-loaded IMAC columns (HisTrap, GE Healthcare/Cytiva) equilibrated with at least 5 column volumes of IMAC binding buffer were loaded with protein lysates under a flow rate of 1 mL/min. His-tagged protein was then eluted by a gradient over 30 min, flow rate 0.5 mL/min from 0% to 100% IMAC elution buffer (20 mM sodium phosphate, 0.5 M NaCl, 0.5 M imidazole, pH 7.2). During elution, samples were collected in fractions of 0.5 mL and protein content monitored via an UV-detector at 280 nm. Protein-containing fractions were combined and purified further via SEC on a Superdex 75 10/300 GL column (GE Healthcare/Cytiva) using 20 mM sodium phosphate

buffer, pH 7.2, a buffer condition previously reported to preserve MIF bioactivity (*64*). Protein-containing and imidazole-free fractions were collected and sterile-filtered over a 0.2 µm filter prior to further use. Protein purity was assessed by sodium dodecylsulfate-polyacrylamide gel electrophoresis (SDS-PAGE) with Coomassie and silver staining as well as anti-6xHis immunoblot (see below). Endotoxin content of every batch of protein was measured photometrically in sterile-filtered protein solution using the Pierce LAL Chromogenic Endotoxin Quantitation Kit (Thermo Fisher Scientific, Dreieich, Germany) essentially following the manufacturer's instruction. Purified protein was stored at 4 ºC and used within a maximum of 4 weeks.

Protein crystallization and structure determination

For crystallization, buffers of all MDL proteins were exchanged for 20 mM HEPES, 250 mM NaCl, pH 7.5, immediately after purification and the protein was then concentrated (MDL1: 12.3 mg/mL, MDL2: 11.1 mg/mL, MDL3: 9.8 mg/mL). For all MDL proteins, crystallization experiments were carried out using sitting drop/vapor diffusion crystallization in a 200 nL + 200 nL format using a Phoenix crystallization robot in MRC-2 crystallization plates. Individual crystallization conditions for MDL1 consisted of 50 mM Tris, pH 8.0, 0.2 M calcium acetate, and 26% PEG 8000. For MDL2, the crystallization conditions were 50 mM Tris, pH 8.0, and 2.25 M ammonium sulfate; and for MDL3 they were 50 mM MES, pH 6.0, 4% MPD, 0.2 M ammonium acetate, and 30% PEG3350. All crystals were grown at 292.15 K. For cryoprotection, individual crystals were transferred to a new drop containing the mother liquor enriched with 30% ethylene glycol for MDL1, 30% glycerol for MDL2, and 30% ethylene glycol for MDL3,

and flash-frozen in liquid nitrogen. X-ray data were collected at 100 K at the Paul Scherrer Institute (PSI) synchrotron using a Dectris Eiger2 16M Detector (wavelength=0.9999 Å).

Diffraction data reduction was done using the XDS program (*65*). The observed reflections were scaled and merged using Aimless (*66*) provided in the CCP4 software. The crystal structures were solved with human MIF monomer by molecular replacement using Phaser (*67*). The structure solution yielded a trimer in the asymmetric unit for MDL1 and MDL2 and a monomer for MDL3. The refinement of the structures was performed using the module Phenix.refine (*68*) of the PHENIX package. Cycles of refinement and model building were performed using Phenix.refine and Coot (*69*). The stereochemistry of these crystal structures was assessed using MOLPROBITY (*70*). Individual refinement statistics for each protein are listed in table S1. Structural data for MDL1, MDL2, and MDL3 were collected at 1.56 Å, 1.40 Å, and 2.0 Å resolution, respectively. The crystal structures were compared to each other and to the previously published MIF structure (PDB 3DJH; (*71*)) using PyMOL and Chimera software for visualization and analysis (*72*).

Generation of monoclonal antibodies recognizing MDL1

Lou/c rats were immunized with 60 µg purified full-length MDL1-6xHis protein, 5 nmol CpG (TIB MOLBIOL, Berlin, Germany), and an equal volume of Incomplete Freund's adjuvant (IFA; Sigma, St. Louis, USA). Hybridoma supernatants were generated and screened as described previously (*34*). Selected supernatants were validated by slot blot immunoassay on recombinant purified human MIF (MIF), human MIF-2/D-DT, and the three MDL proteins for specificity and

sensitivity (fig. S5). Hybridoma cells from clone ATM1 21G9 (IgG2b/ƙ) were subcloned twice by limiting dilution to obtain a stable monoclonal antibody-producing cell line.

SDS-PAGE and immunoblot analysis of recombinant MDL-6xHis proteins

Following purification, protein purity was assessed via SDS-PAGE and Coomassie staining or silver staining and immunoblotting was performed with an antibody recognizing hexahistidine tags. Electrophoresis was performed in 15% acrylamide gels under reducing conditions as described before (*36*). For immunoblot analysis, electrophoresed proteins were transferred to nitrocellulose membranes using Tris-glycine transfer buffer (Thermo Fisher Scientific), followed by blocking (1% BSA) and staining in TBST (Tris-buffered saline, 150 mM NaCl, 20 mM Tris, 0.01% Tween-20, pH 7.3) supplemented with 1% bovine serum albumin (BSA) (Sigma-Aldrich). Hexahistidine-tagged proteins were then detected using a murine monoclonal antibody specific for 6xHis tag (Ma1-135, Invitrogen, Karlsruhe, Germany) as primary antibody and revealed by horseradish peroxidase (HRP)-conjugated goat anti-mouse IgG (ab6789, Abcam, Cambridge, UK). Imaging was performed upon addition of SuperSignal™ West Dura Extended Duration Substrate (Thermo Fisher Scientific) on an Odyssey Fc Imaging System using ImageStudioTM software (LICOR Biosciences, Bad Homburg, Germany).

Coimmunoprecipitation

Prior to immunoprecipitation, MIF-6xHis was biotinylated using a commercial biotin labeling kit (Roche Diagnostics GmbH, Mannheim, Germany), performed essentially as per manufacturer's instructions. For biotinylation, 1 mg recombinant MIF-6xHis at a concentration of 1 mg/mL in

20 mM sodium phosphate buffer, pH 7.2, was used. Coimmunoprecipitation experiments were then carried out using Dynabeads™ M-280 streptavidin (Thermo Fisher Scientific). To this end, 800 µg of recombinant proteins (biotin-MIF-6xHis and/or MDL1-6xHis) were mixed in a total volume of 100 µL PBS, pH 7.4 and incubated overnight at 4 °C to allow time for interaction. Beads were resuspended thoroughly and 20 µL beads were washed with 0.5 mL washing buffer (PBS, 0. 1% Tween 20, pH 7.4). Following magnetic isolation, beads were resuspended in the protein mixture and incubated with slight agitation for 2 h at room temperature. Thereafter, beads and all protein bound to them were magnetically isolated for 3 min, with the supernatant then removed. Beads were washed 3 times with 0.5 mL washing buffer, resuspended in 40 µL denaturing SDS-PAGE sample buffer containing DTT as reducing agent and boiled for 5 min at 95 °C. Protein samples were magnetically separated from the beads prior to analysis by SDS-PAGE.

After blotting, biotin-MIF-6×His was revealed via its biotin-tag using streptavidin-POD-conjugate (Roche Diagnostics GmbH, Mannheim, Germany; 1:1000 dilution), while MDL1-6×His was revealed either via its hexahistidine-tag using a HPR-conjugated antibody specific for the 6×His-tag (GeneTex Inc., USA; 1:1000 dilution) or by a custom-made antibody specific for MDL1 (clone ATM1 21G9, see above). This custom-made antibody was used in form of a 1:10 dilution of hybridoma supernatant as a primary antibody, in combination with a mouse-derived, HRP-conjugated secondary antibody specific for rat IgG2b immunoglobulins (1:1000 dilution). Where necessary, antibodies were removed from membranes by a 10 min incubation in Restore™ PLUS Western blot stripping buffer (Invitrogen) and membranes were again blocked with 1% BSA in TBST, followed by incubation with the respective antibodies. Imaging was performed on an Odyssey Fc Imaging System using ImageStudio™ software (LICOR

Biosciences, Bad Homburg, Germany), using SuperSignal™ West Femto Maximum Sensitivity Substrate (Thermo Fisher Scientific).

Yeast two-hybrid binding assay

For yeast two-hybrid assay, Gateway® cloning-compatible vectors pDEST32 and pDEST22 (Invitrogen ProQuest yeast two-hybrid System) were used, which enable N-terminal fusions of bait and prey proteins with the Gal4 activation- and DNA-binding domains, respectively. *MIF* and *MDL* coding sequences were mobilized from pDONR207 entry clones via Gateway® recombination into pDEST32 and pDEST22. The resulting plasmids were transformed into *S. cerevisiae* strain PJ69-4A (*73*). Yeast transformants were dropped on appropriate synthetic complete media lacking selective amino acids for growth control and detecting putative interactions. For drop tests, yeast cultures were grown overnight, washed with sterile water, adjusted to an OD_{600} of 1, ten-fold dilution series established, and 4 µl per strain and dilution dropped onto the corresponding medium. Photographs were taken after 3 d of yeast growth. Bait and prey protein expression was validated by immunoblot analysis using the GAL4 (DBD) (SC-510) and GAL4 (AD) (SC-1663) monoclonal antibodies (Santa Cruz Biotechnology, Dallas, TX, USA).

Chemokine receptor signaling assay in yeast

For receptor signaling experiments, we used the functional CXCR4- or CXCR2-expressing transformants of *S. cerevisiae* strain CY12946 that has been previously described (*25*, *42-44*). Briefly, the endogenous yeast pheromone receptor was replaced by human CXCR4 or CXCR2,

respectively, with the activated human chemokine receptor being functionally linked to the downstream MAPK-type signaling pathway, ultimately resulting in expression of the *lacZ/β-gal* reporter gene upon receptor binding. The β-galactosidase enzymatic activity (assessed photometrically) was therefore used as a surrogate parameter for chemokine receptor activation.

An *S. cerevisiae* CY12946 strain lacking CXCR4 was used as a negative control to account for potential background signaling mediated by endogenous yeast proteins or for off-target effects of MIF, MDL1, or CXCL12 not mediated via CXCR4. This strain was generated from the CXCR4-expressing clone by a plasmid loss assay (https://openwetware.org/wiki/McClean:_Plasmid_Loss_Assay; modified from (*46*). A single yeast colony of CY12946-hCXCR4 was grown overnight to saturation in non-selective YPD liquid media. A sub-culture was grown in liquid media to mid-log phase (OD_{600} ~ 0.5) and diluted by 100,000. Of these diluted cells, 200 µl were plated on an YPD agar plate. The culture plate was grown for 3-4 days at 30 °C until the colonies had an appreciable size. A replica of this plate was then made on a selective agar plate in complete minimal (CM) dropout medium (synthetic media -Leu). The replica plate was placed in an incubator at 30 °C for 3 days and compared to the parent to select clones lacking CXCR4 (i.e., clones that lost the ability to grow on the selective medium).

To test for activation of the signaling reporter pathway, yeast cells were grown in a 24-well plate until reaching an OD_{600} of 0.3-0.8 and then incubated with the respective protein samples (MDL1-6×His, MDL2-6×His, MDL3-6×His) or the known agonist MIF-6xHis, either individually or as combinations, either with or without inhibitors added, or with controls as indicated (buffer, CXCL12). A concentration of 10-20 µM protein has previously been shown to create stable responses and was used as a reference point for the inhibitor studies. It must be

noted that, due to the barrier function of the yeast cell wall, high ligand concentrations are needed for stable receptor activation, for example 1-2 µM in the case of CXCL12 (*43*). Activation of chemokine receptors was detected by measuring ß-galactosidase activity using the commercially available Beta-Glo assay system (Promega Corp, Madison, WI, USA) and the luminescence signal was recorded on a multimodal plate reader (Enspire 2300, PerkinElmer Life Sciences, Rodgau, Germany). The kit was used as per manufacturer's instructions and is based on coupling ß-galactosidase enzymatic activity to a luciferase reaction. After mixing assay buffer and assay substrate in a 1:1 ratio, a volume of this mixture equal to the media volume was added to each well. After mixing and incubation at room temperature for 30 min, luminescence of each sample was measured.

Luciferase complementation imaging (LCI) assays

For LCI assays, Gateway® cloning-compatible vectors pAMPAT-nLUC-GWY and pAMPAT-cLUC-GWY (*34*) were used, which enable N-terminal fusions of bait and prey proteins with the N- and C-terminal segments of firefly luciferase, respectively. *MIF* and *MDL* coding sequences were mobilized from pDONR207 entry clones via Gateway® recombination into pAMPAT-nLUC-GWY and pAMPAT-cLUC-GWY. The resulting plasmids were transformed into *A. tumefaciens* strain GVG3101 (pMP90RK). Bacterial cultures were grown overnight, resuspended in infiltration media (10 mM MES, pH 5.6, 10 mM $MgCl_2$, 200 µM acetosyringone) to an OD_{600} of 0.5 and incubated at room temperature for 2 h. For co-infiltration, equal volumes of each *A. tumefaciens* transformant were mixed and infiltrated with a needleless syringe from the abaxial

side into fully expanded leaves of four- to six-week-old *N. benthamiana* plants. The leaves were sprayed with 1 mM D-luciferin (PerkinElmer) solved in water supplemented with 0.01% (v/v) Tween-20 at three days after infiltration. Leaves were kept in the dark for 10 min before luminescence was detected with a ChemiDoc™ XRS+ imagine system (Bio-Rad, Feldkirchen, Germany). Luminescence intensities/mm^2 infiltrated leaf area of different combinations were evaluated using the Image Lab software (BioRad, version 6.1). For each combination of interaction partners, three independent experiments consisting of two different plants and two leaves per plant were evaluated. *Agrobacterium*-mediated transient expression of LCI constructs in *N. benthamiana* was validated by immunoblot analysis using a polyclonal primary antibody specific for luciferase (Merck, diluted 1:1000).

Primary human neutrophils and chemotaxis

Blood was obtained from healthy human volunteers (ethics approval LMU Munich, Germany; AZ 18-104). After red blood cell lysis and removal of the supernatant, the neutrophil pellet was gently resuspended in RPMI media (Invitrogen/Gibco, Karlsruhe, Germany) supplemented with 10% heat-inactivated fetal calf serum (FCS) and 1% penicillin/streptomycin. Flow cytometric analysis of neutrophils using characteristic forward/side scatter (FSC/SSC) verified a purity of 98-99%. Isolated primary human neutrophils were kept at room temperature and were used immediately after isolation.

For Transwell migration, freshly isolated neutrophils in RPMI without supplements were set up to migrate for 4 h over a membrane with a pore size of 5 μm (Corning Inc. New York, USA).

Lower chambers were filled with 600 µL RPMI containing chemokines/treatments and inhibitors according to the respective experimental design. Transwell plates were incubated at 37°C for 30 min to allow prewarming of medium and plate. Then, 100 µL of cell suspension containing 1×10^6 cells in RPMI were carefully added to the upper chambers of a Transwell insert after placing the filters onto the lower chambers.

The 3D-gel-matrix chemotaxis assay was performed using commercially available Ibidi µ-slides (Ibidi GmbH, Gräfelfing, Germany) with a tissue-like collagen matrix, allowing to study cell migration under native-like conditions. Live-cell imaging, time-lapse microscopy and single-cell tracking allow for measuring a variety of chemotactic parameters, complementing the end-point results obtained in Transwell migration experiments. To this end, 8×10^6 cells/100 µL in RPMI without supplements were prepared and used immediately. The collagen gel matrix was prepared at a final collagen concentration of 1 mg/mL, with all components handled on ice to ensure slow gel polymerization. Then, 6.3 µL of collagen-cell suspension were added to the appropriate filling ports. Afterwards, all filling ports were closed with dedicated plugs and gels incubated at 37°C and 5% CO_2 for 30 min to allow solidification of the collagen matrix. Channels were checked microscopically and only perfectly filled channels were used in the experiment. After matrix preparation, 65 µL of chemoattractant-free, RPMI was added to the chamber on one side of the matrix and 65 µL of chemoattractant-containing RPMI media was added to the other side. This created a native chemoattractant gradient over the cell-containing gel-matrix. Immediately after adding treatments, slides were installed on a motorized and pre-heated microscopy stage. Automated time-lapse microscopy was performed for 2 h at a time-interval of 1 min on a Leica inverted DMi8-Life Cell Imaging System equipped with a DMC2900 Digital Microscope Camera with CMOS sensor and live cell-imaging software (Leica Microsystems, Wetzlar,

Germany). Images were imported as stacks to ImageJ software and analyzed with the manual tracking extension and the chemotaxis/migration tools from Ibidi GmbH.

AKT signaling pathway analysis

The MIF-CXCR4-PI3K-AKT axis is a well-studied MIF response pathway, implicated among others in cell survival, migration, and cancer development (*57, 74*). A549 cells were obtained from the German Collection of Microorganisms and Cell Cultures GmbH (DSMZ) and maintained in Ham's F-12K Medium (Invitrogen/Gibco) supplemented with 10% FCS and 1% penicillin/streptomycin (Sigma-Aldrich, Deisenhofen, Germany). Cells were plated in 150 cm^2 cell culture flasks and cultured at 37°C in a humidified atmosphere containing 5% CO_2. Culture medium was changed every two days. Cells were subcultured before reaching confluency using a 0.1% trypsin solution in EDTA (Sigma-Aldrich). Cells were split 1:10 during each passage, with passages used in this study ranging from 3-10. Cells were treated with MIF, MDL1 or the combination of the two (1:1 ratio), each at a final concentration of 16 nM. After 10 min incubation, treated cells were lysed in NuPAGE™ lithium dodecyl sulfate/dithiothreitol lysis buffer including PhosphoSTOP™ reagent (Roche Applied Science, Mannheim, Germany). Lysates were run in 11% SDS-PAGE gels and blotted onto nitrocellulose membrane. Immunoblots were developed with antibodies specific for phosphorylated (pAKT; ab81283, Abcam, Cambridge, UK) and total (ab8805, Abcam) AKT, as well as an antibody directed against β-actin (ab8227, Abcam) as an internal reference. Respective HRP-conjugated secondary antibodies (211-032-171, Jackson ImmunoResearch, Ely, UK) were used for detection. Imaging and densitometric band quantification were performed upon addition of SuperSignal™ West Dura Extended Duration Substrate (ThermoFisher Scientific) on an Odyssey Fc Imaging System

using ImageStudio™ software (LICOR Biosciences, Bad Homburg, Germany). Densitometric quantification was done by normalizing both total AKT and pAKT to β-actin, and then comparing the amount of normalized pAKT to normalized AKT.

Isolation of messenger RNA (mRNA), reverse transcription and quantitative real-time polymerase chain reaction (RT-qPCR) in A549 cells

For RT-qPCR, 1×10^6 A549 cells were seeded in 6 well plates and grown as described above until they reached confluency. Cells were treated with recombinant proteins for 4 h at the indicated concentrations. mRNA was extracted using TRIzol reagent (Invitrogen, Karlsruhe, Germany) as per manufacturer's instructions. mRNA was reverse-transcribed into cDNA using the First Strand cDNA Synthesis Kit (ThermoFisher Scientific) following manufacturer's instructions. RT-qPCR was carried out using the SYBR™ Green PCR Master Mix (ThermoFisher Scientific) on a RotorGene 6000 (Qiagen, Hilden, Germany). The thermal cycling conditions were: initial denaturation at 95°C for 3 min, followed by 40 cycles of 95°C for 10 s and 55°C for 30 s, then followed by 95°C for 1 min and 55°C for 1 min. The fold change was derived by calculating the ratio between each experimental group and control. Ribosomal protein, large, P0 (RPLP0) was used as housekeeping gene for normalization. The relative expression levels were normalized to endogenous control and were expressed as $2^{-\Delta\Delta Ct}$. Primers used for the RT-qPCR experiments are listed in table S2.

Microscale thermophoresis (MST)

All MST experiments were performed on a Monolith NT.115 instrument with green/red filters (NanoTemper Technologies, Munich, Germany). MST and LED power were set at 40% and 60%, respectively, for MDL1 and MDL2, or 40% and 90% for MDL3 measurements to obtain stable fluorescent signals around 1000 fluorescent counts. All measurements were performed at 37 °C with MST traces tracked for 40 s (laser-off: 5 s, laser-on: 30 s; laser-off: 5 s). A stock solution of 200 nM RED-NHS-MIF-6xHis was prepared in 20 mM sodium phosphate buffer, pH 7.4, containing 0.2% BSA, according to the manufacturer's protocol.

For titration of each plant ortholog, each protein sub-stock solution was prepared by serial 1:1 dilution, starting from a 20 µM stock solution in 20 mM sodium phosphate buffer, pH 7.4, 0.1% BSA. RED-NHS-MIF-6xHis and each MDL sub-stock was mixed at a 1:1 ratio resulting in a final MIF concentration of 100 nM and incubated for 10 min in the dark at room temperature. Premium coated capillaries we used as initial screening had shown slight sticking of protein to standard capillary walls. Incubated mixtures were loaded into capillaries and MST measurements started immediately. Obtained MST traces were analyzed at an MST-on time of 1.5 s using the MO.Affinity Analysis version 2.2.4 (NanoTemper Technologies) for each of the three potential interaction pairs. Apparent K_D values were calculated using the same software. Visualization was done using Prism GraphPad (Version 9.4.1) assuming a 1 on 1 binding model with sigmoidal curve fitting models for each set up.

Size Exclusion Chromatography

SEC experiments were performed on an FPLC system (ÄKTA Pure, GE Healthcare/Cytiva, Freiburg, Germany) with a Superdex 75 10/300 GL column (GE Healthcare/Cytiva) using 20

mM sodium phosphate buffer, pH 7.4, and a constant flow of 0.5 mL/min. Proteins were used for SEC one day after purification, either individually or in a 1:1 mixture of MIF-6xHis and MDL1-6xHis, incubated at 4 °C overnight. Proteins were loaded individually, one after another, and peaks observed by UV absorbance (280nm) in mAU over the elution volume in mL. Unicorn 7.0 software (GE Healthcare/Cytiva, Freiburg, Germany) was used to analyze chromatograms for individual elution volumes. Experiments were performed in triplicates.

For the described SEC setup, a standard curve and standard equation was generated using the GE gel filtration calibration kit, LMW (low molecular weight), as per manufacturer's instructions (GE Healthcare/Cytiva). From observed elution volumes and known molecular mass of sample proteins, a standard curve and standard equation were calculated and visualized using Prism GraphPad (Version 9.4.1).

Statistics

Statistical analyses were performed with GraphPad Prism 9 (GraphPad Prism Software Inc., San Diego, CA). After testing for normality by Shapiro-Wilk test, data were analyzed by one-way analysis of variance (ANOVA) followed by *post hoc* comparison with Tukey's test with multiple comparisons, paired t-test with *post hoc* Bonferroni correction, or unpaired t-test, as appropriate. To account for small sample size and potential error in normality tests, appropriate non-parametric tests (Kruskal-Wallis test, Wilcoxon Signed Rank test, Mann-Whitney test, respectively) were performed for comparison and showed similar results. Data are presented as

means ± SD. Considered as significant: $p < 0.05$. Asterisks indicate statistically significant differences as follows: *, $p < 0.05$; **, $p < 0.01$; ***, $p < 0.005$; ****, $p < 0.0001$.

Supplementary Materials

Figs. S1–S17.

Tables S1–S2.

References and Notes

1. C. A. Janeway, Jr., R. Medzhitov, Innate immune recognition. *Annu Rev Immunol* **20**, 197-216 (2002)10.1146/annurev.immunol.20.083001.084359; 083001.084359 [pii]).
2. A. W. Thomson, *The Cytokine Handbook*. (Academic Press, New York NY, USA, ed. 4th edition, 2003).
3. T. Calandra, T. Roger, Macrophage migration inhibitory factor: a regulator of innate immunity. *Nat Rev Immunol* **3**, 791-800 (2003); published online EpubOct (10.1038/nri1200).
4. I. Kang, R. Bucala, The immunobiology of MIF: function, genetics and prospects for precision medicine. *Nat Rev Rheumatol* **15**, 427-437 (2019); published online EpubJul (10.1038/s41584-019-0238-2).
5. A. Kapurniotu, O. Gokce, J. Bernhagen, The multitasking potential of alarmins and atypical chemokines. *Front Med (Lausanne)* **6**, 3 (2019)10.3389/fmed.2019.00003).
6. M. Merk, S. Zierow, L. Leng, R. Das, X. Du, W. Schulte, J. Fan, H. Lue, Y. Chen, H. Xiong, F. Chagnon, J. Bernhagen, E. Lolis, G. Mor, O. Lesur, R. Bucala, The D-dopachrome tautomerase (DDT) gene product is a cytokine and functional homolog of macrophage migration inhibitory factor (MIF). *Proc Natl Acad Sci USA* **108**, E577-585 (2011); published online EpubAugust 4, 2011 (10.1073/pnas.1102941108).
7. L. Leng, C. N. Metz, Y. Fang, J. Xu, S. Donnelly, J. Baugh, T. Delohery, Y. Chen, R. A. Mitchell, R. Bucala, MIF signal transduction initiated by binding to CD74. *J Exp Med* **197**, 1467-1476 (2003); published online EpubJun 2 (10.1084/jem.20030286; jem.20030286 [pii]).
8. J. Bernhagen, R. Krohn, H. Lue, J. L. Gregory, A. Zernecke, R. R. Koenen, M. Dewor, I. Georgiev, A. Schober, L. Leng, T. Kooistra, G. Fingerle-Rowson, P. Ghezzi, R. Kleemann, S. R. McColl, R. Bucala, M. J. Hickey, C. Weber, MIF is a noncognate ligand of CXC chemokine receptors in inflammatory and atherogenic cell recruitment. *Nat Med* **13**, 587-596 (2007).
9. E. F. Morand, M. Leech, J. Bernhagen, MIF: a new cytokine link between rheumatoid arthritis and atherosclerosis. *Nat Rev Drug Discov* **5**, 399-411 (2006); published online EpubApr 21
10. A. Zernecke, J. r. Bernhagen, C. Weber, Macrophage migration inhibitory factor in cardiovascular disease. *Circulation* **117**, 1594-1602 (2008).
11. H. Conroy, L. Mawhinney, S. C. Donnelly, Inflammation and cancer: macrophage migration inhibitory factor (MIF)--the potential missing link. *QJM*, hcq148 (2010); published online Epub2010 (10.1093/qjmed/hcq148).
12. M. Sauler, R. Bucala, P. J. Lee, Role of macrophage migration inhibitory factor in age-related lung disease. *Am J Physiol Lung Cell Mol Physiol* **309**, L1-10 (2015); published online EpubJul 1 (10.1152/ajplung.00339.2014).
13. P. V. Tilstam, D. Qi, L. Leng, L. Young, R. Bucala, MIF family cytokines in cardiovascular diseases and prospects for precision-based therapeutics. *Expert opinion on therapeutic targets* **21**, 671-683 (2017); published online EpubJul (10.1080/14728222.2017.1336227).
14. M. F. Leyton-Jaimes, J. Kahn, A. Israelson, Macrophage migration inhibitory factor: A multifaceted cytokine implicated in multiple neurological diseases. *Exp Neurol* **301**, 83-91 (2018); published online EpubMar (10.1016/j.expneurol.2017.06.021).

15. R. Panstruga, S. C. Donnelly, J. Bernhagen, A cross-kingdom view on the immunomodulatory role of MIF/D-DT proteins in mammalian and plant Pseudomonas infections. *Immunology* **166**, 287-298 (2022); published online EpubJul (10.1111/imm.13480).
16. A. Sparkes, P. De Baetselier, K. Roelants, C. De Trez, S. Magez, J. A. Van Ginderachter, G. Raes, R. Bucala, B. Stijlemans, Reprint of: The non-mammalian MIF superfamily. *Immunobiology* **222**, 858-867 (2017); published online EpubJun (10.1016/j.imbio.2017.05.004).
17. C. Michelet, E. G. J. Danchin, M. Jaouannet, J. Bernhagen, R. Panstruga, K. H. Kogel, H. Keller, C. Coustau, Cross-Kingdom Analysis of Diversity, Evolutionary History, and Site Selection within the Eukaryotic Macrophage Migration Inhibitory Factor Superfamily. *Genes (Basel)* **10**, 740 (2019); published online EpubSep 24 (10.3390/genes10100740).
18. S. H. Spoel, X. Dong, How do plants achieve immunity? Defence without specialized immune cells. *Nat Rev Immunol* **12**, 89-100 (2012); published online EpubJan 25 (10.1038/nri3141).
19. H. W. Sun, J. Bernhagen, R. Bucala, E. Lolis, Crystal structure at 2.6-A resolution of human macrophage migration inhibitory factor. *Proc Natl Acad Sci USA* **93**, 5191-5196. (1996).
20. G. Poelarends, V. Veetil, C. Whitman, The chemical versatility of the β–α–β fold: Catalytic promiscuity and divergent evolution in the tautomerase superfamily. *Cell Mol Life Sci* **65**, 3606-3618 (2008)10.1007/s00018-008-8285-x).
21. E. Rosengren, P. Aman, S. Thelin, C. Hansson, S. Ahlfors, P. Bjork, L. Jacobsson, H. Rorsman, The macrophage migration inhibitory factor MIF is a phenylpyruvate tautomerase. *FEBS letters* **417**, 85-88. (1997).
22. E. Rosengren, R. Bucala, P. Aman, L. Jacobsson, G. Odh, C. N. Metz, H. Rorsman, The immunoregulatory mediator macrophage migration inhibitory factor (MIF) catalyzes a tautomerization reaction. *Molecular medicine (Cambridge, Mass.)* **2**, 143-149. (1996).
23. M. Swope, H. W. Sun, P. R. Blake, E. Lolis, Direct link between cytokine activity and a catalytic site for macrophage migration inhibitory factor. *EMBO J* **17**, 3534-3541. (1998).
24. C. Fan, D. Rajasekaran, M. A. Syed, L. Leng, J. P. Loria, V. Bhandari, R. Bucala, E. J. Lolis, MIF intersubunit disulfide mutant antagonist supports activation of CD74 by endogenous MIF trimer at physiologic concentrations. *Proc Natl Acad Sci USA* **110**, 10949-10949 (2013); published online EpubJun 17 (10.1073/pnas.1221817110).
25. D. Rajasekaran, S. Groning, C. Schmitz, S. Zierow, N. Drucker, M. Bakou, K. Kohl, A. Mertens, H. Lue, C. Weber, A. Xiao, G. Luker, A. Kapurniotu, E. J. Lolis, J. Bernhagen, Macrophage Migration Inhibitory Factor-CXCR4 Receptor Interactions: Evidence for Partial Allosteric Agonism in Comparison to CXCL12. *The Journal of biological chemistry*, (2016); published online EpubMay 19 (10.1074/jbc.M116.717751).
26. G. Pantouris, J. Ho, D. Shah, M. A. Syed, L. Leng, V. Bhandari, R. Bucala, V. S. Batista, J. P. Loria, E. J. Lolis, Nanosecond Dynamics Regulate the MIF-Induced Activity of CD74. *Angew Chem Int Ed Engl* **57**, 7116-7119 (2018); published online EpubApr 18 (10.1002/anie.201803191).
27. G. Pantouris, M. A. Syed, C. Fan, D. Rajasekaran, T. Y. Cho, E. M. Rosenberg, Jr., R. Bucala, V. Bhandari, E. J. Lolis, An Analysis of MIF Structural Features that Control Functional Activation of CD74. *Chemistry & biology* **22**, 1197-1205 (2015); published online EpubSep 17 (10.1016/j.chembiol.2015.08.006).

28. Y. Cho, G. V. Crichlow, J. J. Vermeire, L. Leng, X. Du, M. E. Hodsdon, R. Bucala, M. Cappello, M. Gross, F. Gaeta, K. Johnson, E. J. Lolis, Allosteric inhibition of macrophage migration inhibitory factor revealed by ibudilast. *Proc Natl Acad Sci USA* **107**, 11313-11318 (2010); published online EpubJune 22, 2010 (10.1073/pnas.1002716107).
29. M. Brandhofer, J. Bernhagen, Cytokine aerobics: Oxidation controls cytokine dynamics and function. *Structure* **30**, 787-790 (2022); published online EpubJun 2 (10.1016/j.str.2022.05.005).
30. Y. Wang, R. An, G. K. Umanah, H. Park, K. Nambiar, S. M. Eacker, B. Kim, L. Bao, M. M. Harraz, C. Chang, R. Chen, J. E. Wang, T.-I. Kam, J. S. Jeong, Z. Xie, S. Neifert, J. Qian, S. A. Andrabi, S. Blackshaw, H. Zhu, H. Song, G.-l. Ming, V. L. Dawson, T. M. Dawson, A nuclease that mediates cell death induced by DNA damage and poly(ADP-ribose) polymerase-1. *Science* **354**, (2016)10.1126/science.aad6872).
31. R. Panstruga, K. Baumgarten, J. Bernhagen, Phylogeny and evolution of plant macrophage migration inhibitory factor/D-dopachrome tautomerase-like proteins. *BMC evolutionary biology* **15**, 64 (2015)10.1186/s12862-015-0337-x).
32. C. Weber, S. Kraemer, M. Drechsler, H. Lue, R. R. Koenen, A. Kapurniotu, A. Zernecke, J. Bernhagen, Structural determinants of MIF functions in CXCR2-mediated inflammatory and atherogenic leukocyte recruitment. *Proc Natl Acad Sci USA* **105**, 16278-16283 (2008); published online EpubOctober 21, 2008 (10.1073/pnas.0804017105).
33. Y. Cho, B. F. Jones, J. J. Vermeire, L. Leng, L. DiFedele, L. M. Harrison, H. Xiong, Y. K. Kwong, Y. Chen, R. Bucala, E. Lolis, M. Cappello, Structural and functional characterization of a secreted hookworm Macrophage Migration Inhibitory Factor (MIF) that interacts with the human MIF receptor CD74. *The Journal of biological chemistry* **282**, 23447-23456 (2007); published online EpubAug 10 (
34. K. Gruner, F. Leissing, D. Sinitski, H. Thieron, C. Axstmann, K. Baumgarten, A. Reinstadler, P. Winkler, M. Altmann, A. Flatley, M. Jaouannet, K. Zienkiewicz, I. Feussner, H. Keller, C. Coustau, P. Falter-Braun, R. Feederle, J. Bernhagen, R. Panstruga, Chemokine-like MDL proteins modulate flowering time and innate immunity in plants. *J Biol Chem* **296**, 100611 (2021); published online EpubJan-Jun (10.1016/j.jbc.2021.100611).
35. X. Robert, P. Gouet, Deciphering key features in protein structures with the new ENDscript server. *Nucleic Acids Res* **42**, W320-324 (2014); published online EpubJul (10.1093/nar/gku316).
36. D. Sinitski, K. Gruner, M. Brandhofer, C. Kontos, P. Winkler, A. Reinstadler, P. Bourilhon, Z. Xiao, R. Cool, A. Kapurniotu, F. J. Dekker, R. Panstruga, J. Bernhagen, Cross-kingdom mimicry of the receptor signaling and leukocyte recruitment activity of a human cytokine by its plant orthologs. *J Biol Chem* **295**, 850-867 (2020); published online EpubJan 17 (10.1074/jbc.RA119.009716).
37. Y. Cho, J. J. Vermeire, J. S. Merkel, L. Leng, X. Du, R. Bucala, M. Cappello, E. Lolis, Drug repositioning and pharmacophore identification in the discovery of hookworm MIF inhibitors. *Chem Biol* **18**, 1089-1101 (2011); published online EpubSep 23 (10.1016/j.chembiol.2011.07.011).
38. E. Naessens, G. Dubreuil, P. Giordanengo, O. L. Baron, N. Minet-Kebdani, H. Keller, C. Coustau, A Secreted MIF Cytokine Enables Aphid Feeding and Represses Plant Immune Responses. *Curr Biol* **25**, 1898-1903 (2015); published online EpubJul 20 (10.1016/j.cub.2015.05.047).

39. J. B. Lubetsky, A. Dios, J. Han, B. Aljabari, B. Ruzsicska, R. Mitchell, E. Lolis, Y. Al-Abed, The tautomerase active site of macrophage migration inhibitory factor is a potential target for discovery of novel anti-inflammatory agents. *The Journal of biological chemistry* **277**, 24976-24982. (2002).
40. R. Mischke, R. Kleemann, H. Brunner, J. Bernhagen, Cross-linking and mutational analysis of the oligomerization state of the cytokine macrophage migration inhibitory factor (MIF). *FEBS letters* **427**, 85-90 (1998); published online EpubMay 1 (10.1016/s0014-5793(98)00400-1).
41. R. Kleemann, A. Hausser, G. Geiger, R. Mischke, A. Burger-Kentischer, O. Flieger, F. J. Johannes, T. Roger, T. Calandra, A. Kapurniotu, M. Grell, D. Finkelmeier, H. Brunner, J. Bernhagen, Intracellular action of the cytokine MIF to modulate AP-1 activity and the cell cycle through Jab1. *Nature* **408**, 211-216. (2000).
42. A. Sachpatzidis, B. K. Benton, J. P. Manfredi, H. Wang, A. Hamilton, H. G. Dohlman, E. Lolis, Identification of allosteric peptide agonists of CXCR4. *The Journal of biological chemistry* **278**, 896-907. (2003).
43. J. W. Murphy, D. Rajasekaran, J. Merkel, E. Skeens, C. Keeler, M. E. Hodsdon, G. P. Lisi, E. Lolis, High-Throughput Screening of a Functional Human CXCL12-CXCR4 Signaling Axis in a Genetically Modified S. cerevisiae: Discovery of a Novel Up-Regulator of CXCR4 Activity. *Front Mol Biosci* **7**, 164 (2020)10.3389/fmolb.2020.00164).
44. E. M. Rosenberg Jr., R. E. D. Harrison, L. K. Tsou, N. Drucker, B. Humphries, D. Rajasekaran, K. E. Luker, C.-H. Wu, J.-S. Song, C.-J. Wang, J. W. Murray, Y.-C. Cheng, K.-S. Shia, G. D. Luker, D. Morikis, E. J. Lolis, Functional Characterization, Dynamics, and Mechanism of CXCR4 Antagonists on a Constitutively Active Mutant. *Cell Chemical Biology* **26**, 662–673 (2019); published online EpubMay 16, 2019 (
45. M. Lacy, C. Kontos, M. Brandhofer, K. Hille, S. Groning, D. Sinitski, P. Bourilhon, E. Rosenberg, C. Krammer, T. Thavayogarajah, G. Pantouris, M. Bakou, C. Weber, E. Lolis, J. Bernhagen, A. Kapurniotu, Identification of an Arg-Leu-Arg tripeptide that contributes to the binding interface between the cytokine MIF and the chemokine receptor CXCR4. *Scientific reports* **8**, 5171 (2018); published online EpubMar 26 (10.1038/s41598-018-23554-5).
46. V. Lundblad, H. Zhou, Manipulation of plasmids from yeast cells. *Curr Protoc Mol Biol* **Chapter 13**, Unit13.19 (2001); published online EpubMay (10.1002/0471142727.mb1309s39).
47. C. Piette, M. Deprez, T. Roger, A. Noel, J. M. Foidart, C. Munaut, The dexamethasone-induced inhibition of proliferation, migration, and invasion in glioma cell lines is antagonized by macrophage migration inhibitory factor (MIF) and can be enhanced by specific MIF inhibitors. *J Biol Chem* **284**, 32483-32492 (2009); published online EpubNov 20 (
48. J. L. Liang, D. Z. Xiao, X. Y. Liu, Q. X. Lin, Z. X. Shan, J. N. Zhu, S. G. Lin, X. Y. Yu, High glucose induces apoptosis in AC16 human cardiomyocytes via macrophage migration inhibitory factor and c-Jun N-terminal kinase. *Clin Exp Pharmacol Physiol* **37**, 969-973 (2010); published online EpubOct (10.1111/j.1440-1681.2010.05420.x).
49. H. Song, Q. Shen, S. Hu, J. Jin, The role of macrophage migration inhibitory factor in promoting benign prostatic hyperplasia epithelial cell growth by modulating COX-2 and P53 signaling. *Biol Open* **9**, (2020); published online EpubNov 12 (10.1242/bio.053447).

50. L. Schindler, L. Zwissler, C. Krammer, U. Hendgen-Cotta, T. Rassaf, M. B. Hampton, N. Dickerhof, J. Bernhagen, Macrophage migration inhibitory factor inhibits neutrophil apoptosis by inducing cytokine release from mononuclear cells. *J Leukoc Biol* **110**, 893-905 (2021); published online EpubNov (10.1002/JLB.3A0420-242RRR).
51. R. J. Tallarida, Quantitative methods for assessing drug synergism. *Genes Cancer* **2**, 1003-1008 (2011); published online EpubNov (10.1177/1947601912440575).
52. F. Bai, O. A. Asojo, P. Cirillo, M. Ciustea, M. Ledizet, P. A. Aristoff, L. Leng, R. A. Koski, T. J. Powell, R. Bucala, K. G. Anthony, A novel allosteric inhibitor of macrophage migration inhibitory factor (MIF). *Journal of Biological Chemistry* **287**, 30653-30663. (2012); published online EpubJuly 10, 2012 (10.1074/jbc.M112.385583).
53. P. F. Cirillo, O. A. Asojo, U. Khire, Y. Lee, S. Mootien, P. Hegan, A. G. Sutherland, E. Peterson-Roth, M. Ledizet, R. A. Koski, K. G. Anthony, Inhibition of Macrophage Migration Inhibitory Factor by a Chimera of Two Allosteric Binders. *ACS Med Chem Lett* **11**, 1843-1847 (2020); published online EpubOct 8 (10.1021/acsmedchemlett.9b00351).
54. J. S. Philo, T. H. Yang., M. LaBarre, Re-examining the oligomerization state of macrophage migration inhibitory factor (MIF) in solution. *Biophys. Chem.* **108**, 77-87 (2004).
55. L. Cao, X. Wang, X. Liu, W. Meng, W. Guo, C. Duan, X. Liang, L. Kang, P. Lv, Q. Lin, R. Zhang, X. Zhang, H. Shen, Tumor Necrosis Factor α–Dependent Lung Inflammation Promotes the Progression of Lung Adenocarcinoma Originating From Alveolar Type II Cells by Upregulating MIF-CD74. *Laboratory Investigation* **103**, 100034 (2023); published online Epub2023/03/01/ (https://doi.org/10.1016/j.labinv.2022.100034).
56. M. Osaki, M. Oshimura, H. Ito, PI3K-Akt pathway: its functions and alterations in human cancer. *Apoptosis* **9**, 667-676 (2004); published online EpubNov (
57. H. Lue, M. Thiele, J. Franz, E. Dahl, S. Speckgens, L. Leng, G. Fingerle-Rowson, R. Bucala, B. Luscher, J. Bernhagen, Macrophage migration inhibitory factor (MIF) promotes cell survival by activation of the Akt pathway and role for CSN5//JAB1 in the control of autocrine MIF activity. *Oncogene* **26**, 5046-5059 (2007).
58. C. Emontzpohl, C. Stoppe, A. Theissen, C. Beckers, U. P. Neumann, G. Lurje, C. Ju, J. Bernhagen, R. H. Tolba, Z. Czigany, The Role of Macrophage Migration Inhibitory Factor in Remote Ischemic Conditioning Induced Hepatoprotection in a Rodent Model of Liver Transplantation. *Shock* **52**, e124-e134 (2019); published online EpubNov (10.1097/SHK.0000000000001307).
59. J. Khalilpour, S. Roshan-Milani, F. H. Gharalari, A. A. Fard, Macrophage migration inhibitory factor antagonist (p425) ameliorates kidney histopathological and functional changes in diabetic rats. *J Bras Nefrol* **41**, 315-322 (2019); published online EpubJul-Sep (10.1590/2175-8239-JBN-2018-0184).
60. L. Qin, I. Kufareva, L. G. Holden, C. Wang, Y. Zheng, C. Zhao, G. Fenalti, H. Wu, G. W. Han, V. Cherezov, R. Abagyan, R. C. Stevens, T. M. Handel, Crystal structure of the chemokine receptor CXCR4 in complex with a viral chemokine. *Science (New York, N.Y.)* **347**, 1117-1122 (2015); published online EpubMar 6 (10.1126/science.1261064).
61. C. Maaser, L. Eckmann, G. Paesold, H. S. Kim, M. F. Kagnoff, Ubiquitous production of macrophage migration inhibitory factor by human gastric and intestinal epithelium. *Gastroenterology* **122**, 667-680 (2002); published online EpubMar (10.1053/gast.2002.31891).

62. M. Pavlicevic, N. Marmiroli, E. Maestri, Immunomodulatory peptides-A promising source for novel functional food production and drug discovery. *Peptides* **148**, 170696 (2022); published online EpubFeb (10.1016/j.peptides.2021.170696).
63. F. Clement, S. N. Pramod, Y. P. Venkatesh, Identity of the immunomodulatory proteins from garlic (Allium sativum) with the major garlic lectins or agglutinins. *Int Immunopharmacol* **10**, 316-324 (2010); published online EpubMar (10.1016/j.intimp.2009.12.002).
64. J. Bernhagen, R. A. Mitchell, T. Calandra, W. Voelter, A. Cerami, R. Bucala, Purification, bioactivity, and secondary structure analysis of mouse and human macrophage migration inhibitory factor (MIF). *Biochemistry* **33**, 14144-14155 (1994); published online EpubNov 29 (10.1021/bi00251a025).
65. W. Kabsch, XDS. *Acta crystallographica. Section D, Biological crystallography* **66**, 125-132 (2010); published online EpubFeb (10.1107/S0907444909047337).
66. P. R. Evans, G. N. Murshudov, How good are my data and what is the resolution? *Acta Crystallogr D Biol Crystallogr* **69**, 1204-1214 (2013); published online EpubJul (10.1107/S0907444913000061).
67. A. J. McCoy, R. W. Grosse-Kunstleve, P. D. Adams, M. D. Winn, L. C. Storoni, R. J. Read, Phaser crystallographic software. *J Appl Crystallogr* **40**, 658-674 (2007); published online EpubAug 1 (10.1107/S0021889807021206).
68. P. V. Afonine, R. W. Grosse-Kunstleve, N. Echols, J. J. Headd, N. W. Moriarty, M. Mustyakimov, T. C. Terwilliger, A. Urzhumtsev, P. H. Zwart, P. D. Adams, Towards automated crystallographic structure refinement with phenix.refine. *Acta Crystallogr D Biol Crystallogr* **68**, 352-367 (2012); published online EpubApr (10.1107/S0907444912001308).
69. P. Emsley, K. Cowtan, Coot: model-building tools for molecular graphics. *Acta Crystallogr D Biol Crystallogr* **60**, 2126-2132 (2004); published online EpubDec (10.1107/S0907444904019158).
70. V. B. Chen, W. B. Arendall, 3rd, J. J. Headd, D. A. Keedy, R. M. Immormino, G. J. Kapral, L. W. Murray, J. S. Richardson, D. C. Richardson, MolProbity: all-atom structure validation for macromolecular crystallography. *Acta Crystallogr D Biol Crystallogr* **66**, 12-21 (2010); published online EpubJan (10.1107/S0907444909042073).
71. E. F. Pettersen, T. D. Goddard, C. C. Huang, G. S. Couch, D. M. Greenblatt, E. C. Meng, T. E. Ferrin, UCSF Chimera--a visualization system for exploratory research and analysis. *J Comput Chem* **25**, 1605-1612 (2004); published online EpubOct (10.1002/jcc.20084).
72. G. V. Crichlow, J. B. Lubetsky, L. Leng, R. Bucala, E. J. Lolis, Structural and kinetic analyses of macrophage migration inhibitory factor active site interactions. *Biochemistry* **48**, 132-139 (2009); published online EpubJan 13 (10.1021/bi8014423).
73. P. James, J. Halladay, E. A. Craig, Genomic libraries and a host strain designed for highly efficient two-hybrid selection in yeast. *Genetics* **144**, 1425-1436 (1996); published online EpubDec (10.1093/genetics/144.4.1425).
74. L. Garcia-Gerique, M. García, A. Garrido-Garcia, S. Gómez-González, M. Torrebadell, E. Prada, G. Pascual-Pasto, O. Muñoz, S. Perez-Jaume, I. Lemos, N. Salvador, M. Vila-Ubach, A. Doncel-Requena, M. Suñol, A. M. Carcaboso, J. Mora, C. Lavarino, MIF/CXCR4 signaling axis contributes to survival, invasion, and drug resistance of metastatic neuroblastoma cells in the bone marrow microenvironment. *BMC Cancer* **22**, 669 (2022); published online EpubJun 17 (10.1186/s12885-022-09725-8).

Acknowledgements: We thank Elena Conti for making arrangements at the Max-Planck-Institut für Biochemie for X-ray data collection and processing, and Maida Avdic for valuable technical help with the yeast assay. **Funding:** This work was supported by the Deutsche Forschungsgemeinschaft (DFG, German Research Foundation)-Agence Nationale Recherche (ANR) co-funded project "X-KINGDOM-MIF - Cross-kingdom analysis of macrophage migration inhibitory factor (MIF) functions". Respective DFG grants are BE 1977/10-1 to J.B., PA 861/15-1 to R.P. The monoclonal antibody facility and the Division of Vascular Biology of LMU are co-funded by the DFG under Germany´s Excellence Strategy within the framework of the Munich Cluster for Systems Neurology (EXC 2145 SyNergy; ID 390857198), and J.B. also received funding from DFG grant CRC1123/A3. E.L. acknowledges Open Philanthropy for its financial support. L.S. acknowledges receipt of a fellowship from the Studienstiftung des Deutschen Volkes and A.H. acknowledges support from the LMUexc-KTF program of LMU Munich. **Author Contributions:** E.L., J.Be. and R.P. conceived the work; L.S., R.M., F.L., J.Ba., P.B., D.S., S.G., M.B., S.L., L.Z., A.H., B.S., and A.F. performed the experiments; L.S., R.M., J.Ba., and E.L. analyzed the data; L.S. and R.M. composed the figures; D.S., M.B., and R.F. provided critical materials; R.F., A.H., R.P., J.Be., and E.L. provided the funding; L.S., E.L., J.Be., and R.P. wrote and edited the manuscript; all authors reviewed and edited the manuscript. **Competing Interests**: J.Be. is a coinventor on patent applications related to anti-inflammatory strategies to target MIF. All other authors declare that they have no competing interests. **Data and materials availability**: Atomic coordinates and structure factors for MDL1, MDL2, and MDL3 have been deposited at the RCSB PDB (https://www.rcsb.org) under the accession codes 8DQA, 8AP3, and 8DQ6, respectively. All other data needed to evaluate the conclusions in the paper are present in the paper or the Supplementary Materials. The monoclonal antibody ATM1 21G9 recognizing MDL1 is available upon request following completion of a material transfer agreement (MTA).

Figure Legends

Fig. 1. Structural properties of each MDL protein and comparison to MIF. (**A**) Electrostatic surface potential representation of each *Arabidopsis* MDL (MDL1, MDL2, and MDL3) and human MIF. The tautomerase substrate binding sites are marked with dashed circles. Regions of negative potential are colored red, those of positive potential are colored blue, and neutral regions are shown in white and gray. (**B**) Overlays of MDL structures on the structure of the MIF-HPP complex (PDB-1CA7). The blue cartoon represents the structure of MIF. Orange, yellow, and green cartoons represent MDL1, MDL2 and MDL3, respectively. The root-mean-square deviation (RMSD) of atomic positions is shown for each complex. The HPP (red) in these overlays is used as the position of the modelled HPP in the MDL-HPP complexes for analysis. (**C**) Residues of MDL1 analogous to the tautomerase catalytic site of human MIF (orange carbon atoms) superimposed on human MIF (blue carbon atoms from PDB-1CA7) with a modelled HPP substrate. Hydrogen bonds between MIF and HPP (red carbon atoms) are represented by yellow dashed lines, and the aromatic interaction is shown as a black dashed line.

Fig. 2. MIF and MDL proteins interact in vitro, in yeast, and in plant tissues. (**A**) Purified tagged MIF (Biotin-MIF-6×His) and MDL1 (MDL1-6×His) were incubated alone or together, and complexes pulled down by streptavidin-coated beads were blotted after separation by SDS-PAGE. Blots were probed for biotin using a streptavidin-POD-conjugate to visualize MIF and for MDL1 using an MDL1-specific antibody. Input sample before pulldown is shown for comparison. The non-specific band in the pulldown blot probed for MDL1, absent in the input samples, originates from the streptavidin-coated beads used to pull down biotin-tagged MIF and represents streptavidin monomers, which migrate with an apparent molecular mass of 16 kDa in

SDS-PAGE. Pulldown and input samples were blotted on separate membranes for technical reasons. The pulldown experiment shown is representative of two independent experiments (n=2). The pulldown blot was also probed with an antibody specific for the hexahistidine tag (fig. S6). (**B**) Interaction between MIF and MDL proteins in a yeast two-hybrid assay. All possible bait-prey combinations were tested as indicated. Control experiments for growth (left panel) were performed on synthetic complete medium lacking leucine (-L, selection for the bait vector) and tryptophan (-T, selection for the prey vector). Selection for interaction (right panel) was performed on synthetic complete medium lacking leucine (-L), tryptophan (-T), and histidine (-H, selection for interaction); ev, empty vector. For each condition, a 10 × dilution series is shown. Images are representative of three biological replicates (n=3). (**C** and **D**) Interactions between MIF and MDL proteins tested in a luciferase complementation imaging assay in *N. benthamiana* leaves. Representative images (C) show luminescence in representative leaves transfected cLuc-MIF or nLuc-MIF and the indicated nLuc or cLuc MDL fusion constructs, respectively, in discrete areas marked by dashed white circles. Warmer colors indicate a higher amount of luminescence. The white scale bars inside the leaves equal 1 cm. Luminescence was quantified by measuring the intensity of light emission and calculated per square mm (D). The experiment was independently performed three times with four leaves for nLuc-MIF and four leaves for cLuc-MIF in each experiment. Boxplots show the results of the twelve data points per combination (n=12). For statistical analysis, paired t test with *post hoc* Bonferroni correction was conducted accounting for correlations among intensity measurements on the same leaf. (**E**) Direct protein–protein interaction studies between fluorescently labeled RED-NHS-MIF and MDL proteins using microscale thermophoresis (MST). For a constant MIF concentration of 100 nM, the difference in normalized fluorescence [‰] is plotted against

increasing MDL concentrations for analysis of thermophoresis. Values shown represent means ± SD as obtained from at least three biologically independent experiments (n ≥3).

Fig. 3. ~~Synergistic effect of MIF and MDL proteins on human chemokine receptor activation in a yeast-based reporter system.~~ MDL1 and MDL2 activate CXCR2 and CXCR4 in yeast and synergize with MIF We measured the activation of CXCR2 and CXCR4 by recombinant MIF, MDL1, and MDL2, alone or in combination, and in the absence or presence of specific inhibitors, in a yeast-based reporter system. (**A**) Schematic illustration of the modified pheromone signaling pathway in *S. cerevisiae.* The endogenous GPCR Ste2 has been replaced by the human chemokine receptor CXCR2 or CXCR4 and linked to the Ste2 downstream signaling cascade. Ligand binding results in activation of the MAPK pathway and eventually triggers expression of the *lacZ* reporter gene. The resulting β-galactosidase activity was measured using a luminescence assay. (**B and C**) Quantification of luminescence (in relative light units, RLU) 30 minutes after the addition of recombinant proteins to the CXCR4 (B) or CXCR2 (C) yeast reporter system. MIF and MDLs were used either individually or mixed 1:1 for a final total concentration of 20 µM protein per treatment. (**D to F**) Quantification of luminescence in CXCR4 or CXCR2 reporter cells stimulated with MIF, MDL1, and MDL2 as indicated in the absence or presence of 100 µM ISO-1 (D), 100 µM AMD3100 (E), or 200 µM SB225002 (F). (**G**) Titration experiment in the yeast CXCR4 reporter system. Luminescence was measured in response to increasing concentrations (0, 1, 2, 4 µM) of MDL1 alone or in combination with 20 µM MIF. For comparison, the effect of MIF alone at a concentration of 20 µM is shown. Values shown in (B) to (G) represent means ± SD as obtained from at least three biologically independent experiments (n≥3) with RLUs of each experiment assessed in technical

duplicates and normalized to untreated controls. Individual data points are indicated by white circles. (**H**) Representative concentration-response experiment (H) in the CXCR4 reporter system depicted as bar graph. The graph shows luminescence (in RLU) due to *lacZ* reporter gene activation upon the addition of sub-threshold amounts of MIF (1 µM) and MDL (increasing concentrations 0–10 µM). The response to the endogenous CXCR4 ligand CXCL12 (1 µM) is shown for comparison. Shown are technical triplicates. Two additional biologically independent experiments (n=3), each performed in technical triplicates, are presented in Fig. S10A and S10B, respectively. (**I**) Concentration-response curve for MIF-MDL1 interaction in the CXCR4 reporter system. The curve was modelled based on (H) assuming a non-linear fit and shows a half maximal effective concentration (EC_{50}) of 2.6 µM MDL1 for the synergistic effect. Concentration-response curves modelled based on two additional biologically independent experiments (n=3) are shown in Fig. S10C and S10D, respectively. Statistical analysis was performed using one-way ANOVA with Tukey's multiple comparison (* $p < 0.05$, ** $p < 0.01$, *** $p < 0.001$, **** $p < 0.0001$).

Fig. 4. MIF and MDL1 form hetero-oligomeric complexes in vitro. (**A**) Representative result from size exclusion chromatography (SEC) of MIF-6xHis and MDL1-6xHis applied to the column individually (A) or as a 1:1 mixture (B) in 20 mM sodium phosphate, pH 7.4, at a constant flow rate of 0.5 mL/min. Depicted is the UV absorbance in (milliarbitrary units) mAU over the flow in mL. (**C**) The crystal structure of MIF and p425 showing interactions between two trimers. (**D**) Representative SEC of a MIF, MDL1, and p425 mixture. The positions of the putative hexamer and the trimer are shown. (**E**) Direct protein–protein interaction studies between fluorescently labeled RED-NHS-MIF and MDL1 using microscale thermophoresis

(MST). Inhibitor p425 was used at a 10-fold excess to MIF. For a constant MIF concentration of 100 nM, the difference in normalized fluorescence [given in ‰] is plotted against increasing MDL1 concentrations for analysis of thermophoresis. Values shown represent means ± SD as obtained from at least three biological replicates. (**F**) Quantification of luminescence (in relative light units, RLU) in CXCR4-*lacZ* reporter yeast stimulated with MIF, MDL1, and MDL2 recombinant proteins, alone or in 1:1 combination, at a final total protein concentration of 20 µM, in the absence or presence of 100 µM p425. Values shown represent means ± SD as obtained from at least three independent experiments (n≥3) with RLUs of each experiment assessed in technical duplicates and normalized to untreated controls. Individual data points are indicated by white circles. Statistical analysis was performed using one-way ANOVA with Tukey's post-hoc multiple comparisons test (* $p < 0.05$, **** $p < 0.0001$).

Fig. 5. MDLs promote human neutrophil chemotaxis and augment the chemotactic effect of human MIF. (A) Quantification of chemotactic migration of primary human neutrophils in Transwell chemotaxis assays, presented as the relative migration index, towards different concentrations of MDL1 in the lower chamber. Chemotaxis towards MIF (500 ng/mL) and towards the cognate CXCR2 agonist CXCL8 (10 ng/mL) were included for comparison. Addition of 20 mM sodium phosphate buffer, pH 7.2, to the lower chamber served as negative control to normalize treatments to spontaneous (random) migration. The bars represent means ± SD of 5-7 biological replicates (white circles indicate individual data points). (**B**) Comparison of chemotaxis in response to MIF (500 ng/mL), MDL1 (500 ng/mL), or a 1:1 combination of MIF and MDL1 (250 ng/mL each). CXCL8 (10 ng/mL) served as a positive control, and buffer was the negative control. Bars represent means ± SD of 3-7 biological replicates (white circles

indicate individual data points). (**C to G**) Representative experiments showing 3D chemotaxis of primary human neutrophils as assessed by live-cell microscopy of single-cell migration tracks in the x/y direction in µm. Cells were placed in collagen matrices containing buffer only (control) to track random motility (C) or between a matrix containing buffer and one containing 10 ng/mL CXCL8 (D), 500 ng/mL MIF (E), 500 ng/mL MDL1 (F), or a 1:1 mixture of 250 ng/mL each MIF and MDL1 (G). Orange dots represent the center of mass in each experiment. (**H**) Quantification of results shown in (C to G). The migration tracks of 30 randomly selected cells per treatment group were recorded and the forward migration index plotted (n=30). Statistical analysis was performed using one-way ANOVA with Tukey's posthoc multiple comparison between the buffer control and the treatment groups (* $p < 0.05$, ** $p < 0.01$, *** $p < 0.001$, **** $p < 0.0001$).

Fig. 6. MDL1-mediated neutrophil chemotaxis is inhibited by a CXCR2 inhibitor but not by a CXCR4 inhibitor. (**A**) Quantification of chemotaxis towards various concentrations of MDL1 (100–2000 ng/mL) in Transwell assays in the absence or presence of the CXCR4 inhibitor AMD3100 or the CXCR2 inhibitor SB-225002 as indicated. Migration towards CXCL8 (10 ng/mL) or MIF (500 ng/mL) is shown for comparison, and migration toward 20 mM sodium phosphate buffer, pH 7.2, was used to normalize treatments to random migration (control). The bars represent means ± SD of 3-6 biological replicates (n=3-6), except for the AMD3100 and SB225002 control incubations in the buffer control setting, which are arithmetic means of two independent experiments (n=2). White circles indicate individual data points. (**B and C**) Representative experiments showing 3D chemotaxis of primary human neutrophils as assessed by live-cell microscopy of single-cell migration tracks in the x/y direction in µm. Cells were

placed between a matrix containing buffer only (control) and a matrix containing MIF (500 ng/ml) or MDL1 (500 ng/ml) in the presence of either AMD3100 (B) or SB225002 (C). Orange dots represent the center of mass for each experiment. (**D**) Quantification of the results in (B) and (C) plus experiments in the absence of the inhibitors. The migration tracks of 30 randomly selected cells per treatment group were recorded and the forward migration index plotted (n=30). Statistical analysis was performed using one-way ANOVA with Tukey's posthoc multiple comparison (* $p < 0.05$, ** $p < 0.01$, *** $p < 0.001$, **** $p < 0.0001$).

Fig. 7. MIF and MDL1 synergistically stimulate inflammatory gene expression in A549 lung epithelial cells. (**A**) Analysis of the AKT signaling pathway in A549 lung epithelial cells using immunoblotting for total AKT and phosphorylated (activated) AKT [pAKT(Ser^{473})] following short-term stimulation with MIF (200 ng/mL) or MDL1 (200 ng/mL) or a 1:1 mixture of the two (100 ng/mL each). Untreated control samples were used as negative control. β-actin is a loading control. (**B**) Densitometric quantification of pAKT band intensities in (A) relative to AKT and normalized to β-actin. Bars represent means ± S.D. of 5 biologically independent experiments (white circles indicate individual data points). Statistical analysis was performed using one-way ANOVA with Tukey's posthoc multiple comparison between the untreated control and the treatments. (**C to H**) RT-qPCR analysis of *TNF-α* (C), *IFN-γ* (D), *CCL2* (E), *IL-1β* (F), *IL-6* (G), and *CXCL8* (H) expression in A549 lung epithelial cells after 4 h stimulation with either MIF (100 ng/mL) or MDL 1 (100 ng/mL) or a 1:1 mixrture of MIF and MDL1 (100 ng/mL each). For comparison, stimulation with MIF (200 ng/mL) is shown as well as stimulation with LPS (10 ng/mL, positive control) and 20 mM sodium phosphate buffer, pH 7.2 (buffer control). Transcript abundance is shown as fold change relative to untreated controls and the

housekeeping gene *RPLP0*. Values shown represent means ± SD as obtained from 4-6 biological replicates (black dots indicate individual data points). Statistical analysis was performed using one-way ANOVA with multiple comparison (** $p < 0.01$, **** $p < 0.0001$).

Table 1. Chromatography statistics for SEC of recombinant MIF-6xHis and MDL-6xHis proteins.

Protein	**MIF-6×His**	**MDL1-6×His**	**MDL2-6×His**	**MDL1-6xHis + MIF-6×His[a]**	
Elution Volume V_e [mL][b]	11.71 +/- 0.08	12.39 +/- 0.04	12.67 +/- 0.08	8.673 +/- 0.36	12.33 +/- 0.09
Calculated molecular mass according to V_e [Da][b]	43,831 +/- 731	38,039 +/- 317	35,883 +/- 598	82,543 +/- 6,194	38,518 +/- 723
Predicted monomeric molecular mass [Da][c]	13,410	13,258	13,045	-	-
Ratio calculated/predicted molecular mass	3.27	2.87	2.75	-	-

[a] Note that the two sub-columns represent the two peaks obtained for this protein combination

[b] Values shown represent means ± SD as obtained from at least three independent experiments

[c] Based on the corresponding amino acid sequence.

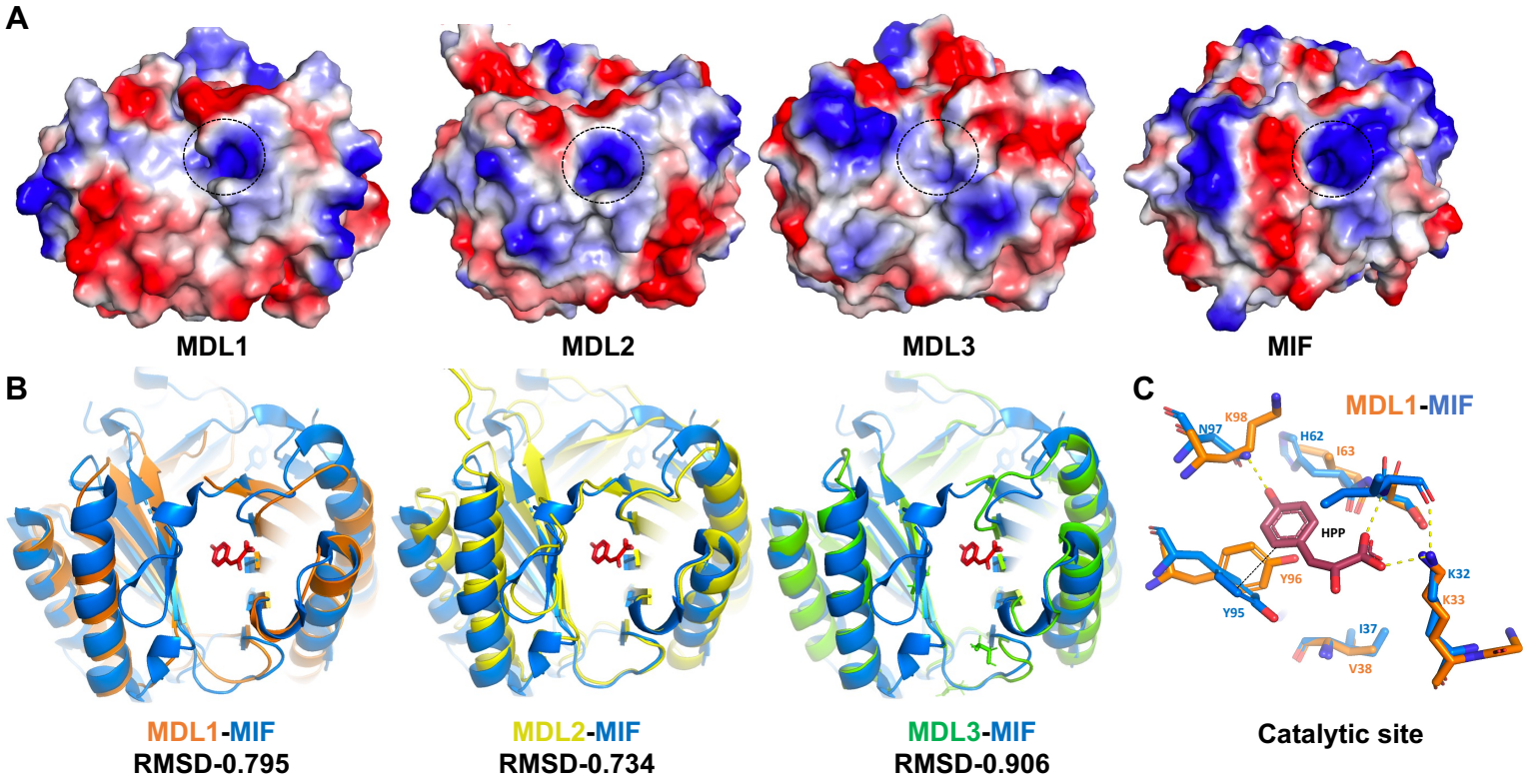
A
MDL1
MDL2
MDL3
MIF
B
MDL1-MIF
RMSD-0.795
MDL2-MIF
RMSD-0.734
MDL3-MIF
RMSD-0.906
C
MDL1-MIF
N97
K98
H62
I63
HPP
Y96
Y95
K32
K33
I37
V38
Catalytic site

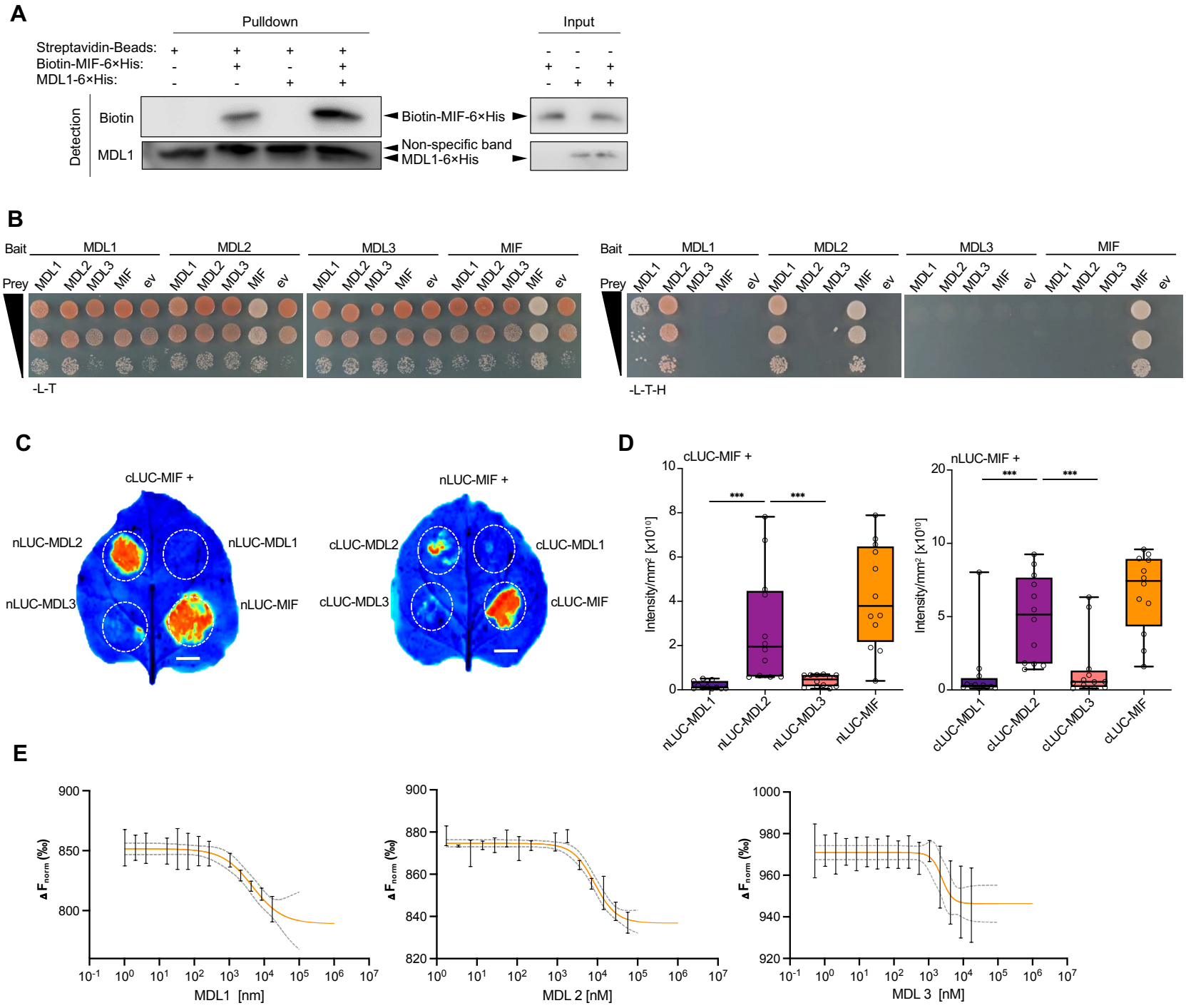
A
Pulldown
Input
Streptavidin-Beads:
Biotin-MIF-6×His:
MDL1-6×His:
Detection
Biotin
MDL1
Biotin-MIF-6×His
Non-specific band
MDL1-6×His
B
Bait
Prey
MDL1
MDL2
MDL3
MIF
ev
-L-T
-L-T-H
C
cLUC-MIF +
nLUC-MDL2
nLUC-MDL1
nLUC-MDL3
nLUC-MIF
nLUC-MIF +
cLUC-MDL2
cLUC-MDL1
cLUC-MDL3
cLUC-MIF
D
cLUC-MIF +
nLUC-MIF +
Intensity/mm² [x10¹⁰]
***
nLUC-MDL1
nLUC-MDL2
nLUC-MDL3
nLUC-MIF
cLUC-MDL1
cLUC-MDL2
cLUC-MDL3
cLUC-MIF
E
ΔF norm (‰)
MDL1 [nm]
MDL 2 [nM]
MDL 3 [nM]

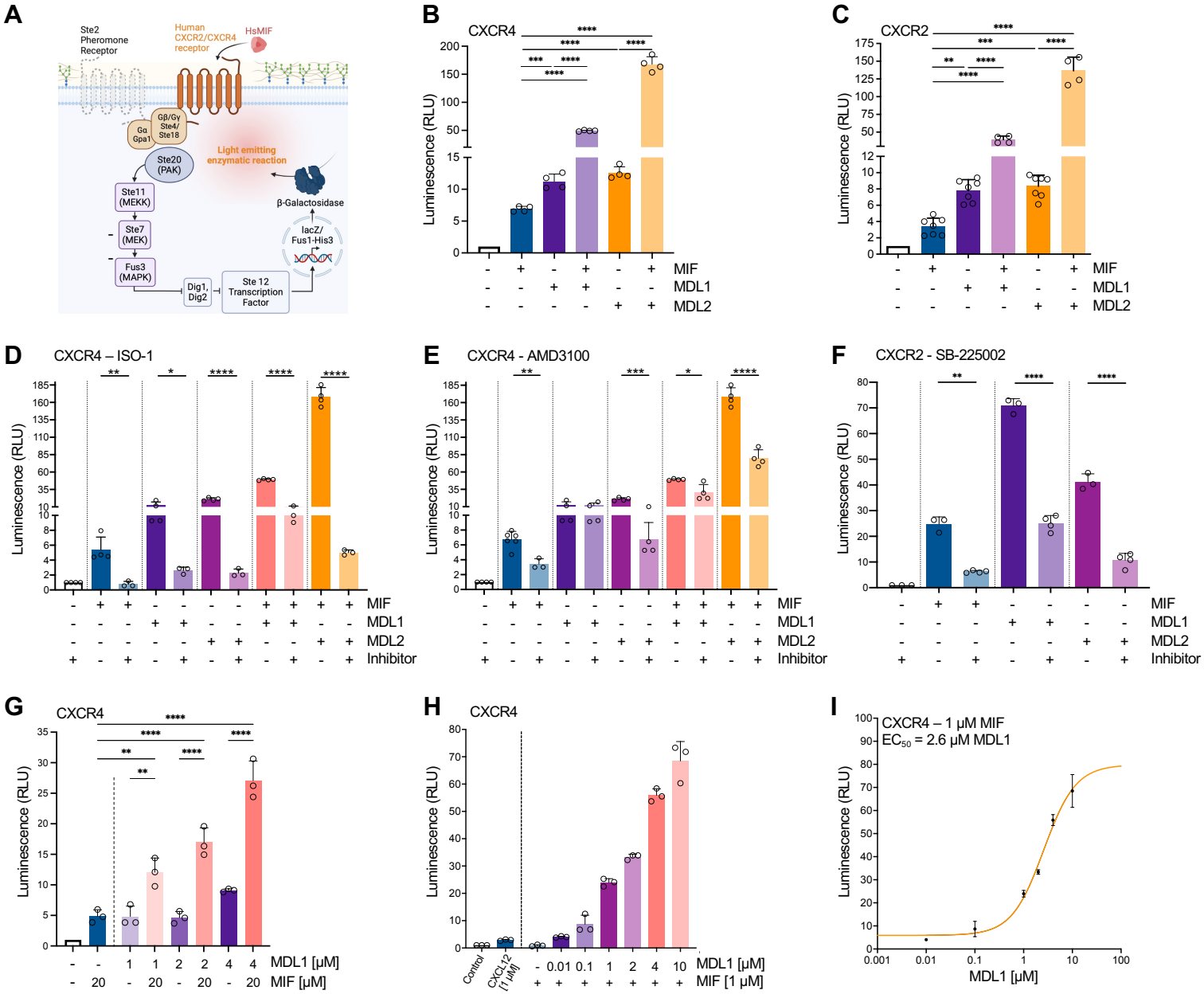
A
Ste2 Pheromone Receptor
Human CXCR2/CXCR4 receptor
HsMIF
Gβ/Gγ Ste4/ Ste18
Gα Gpa1
Ste20 (PAK)
Ste11 (MEKK)
Ste7 (MEK)
Fus3 (MAPK)
Dig1, Dig2
Ste 12 Transcription Factor
Light emitting enzymatic reaction
β-Galactosidase
lacZ/ Fus1-His3
B
CXCR4
Luminescence (RLU)
MIF
MDL1
MDL2
C
CXCR2
D
CXCR4 – ISO-1
Inhibitor
E
CXCR4 - AMD3100
F
CXCR2 - SB-225002
G
CXCR4
MDL1 [μM]
MIF [μM]
H
CXCR4
Control
CXCL12 [1 uM]
MDL1 [μM]
MIF [1 μM]
I
CXCR4 – 1 μM MIF
EC50 = 2.6 μM MDL1

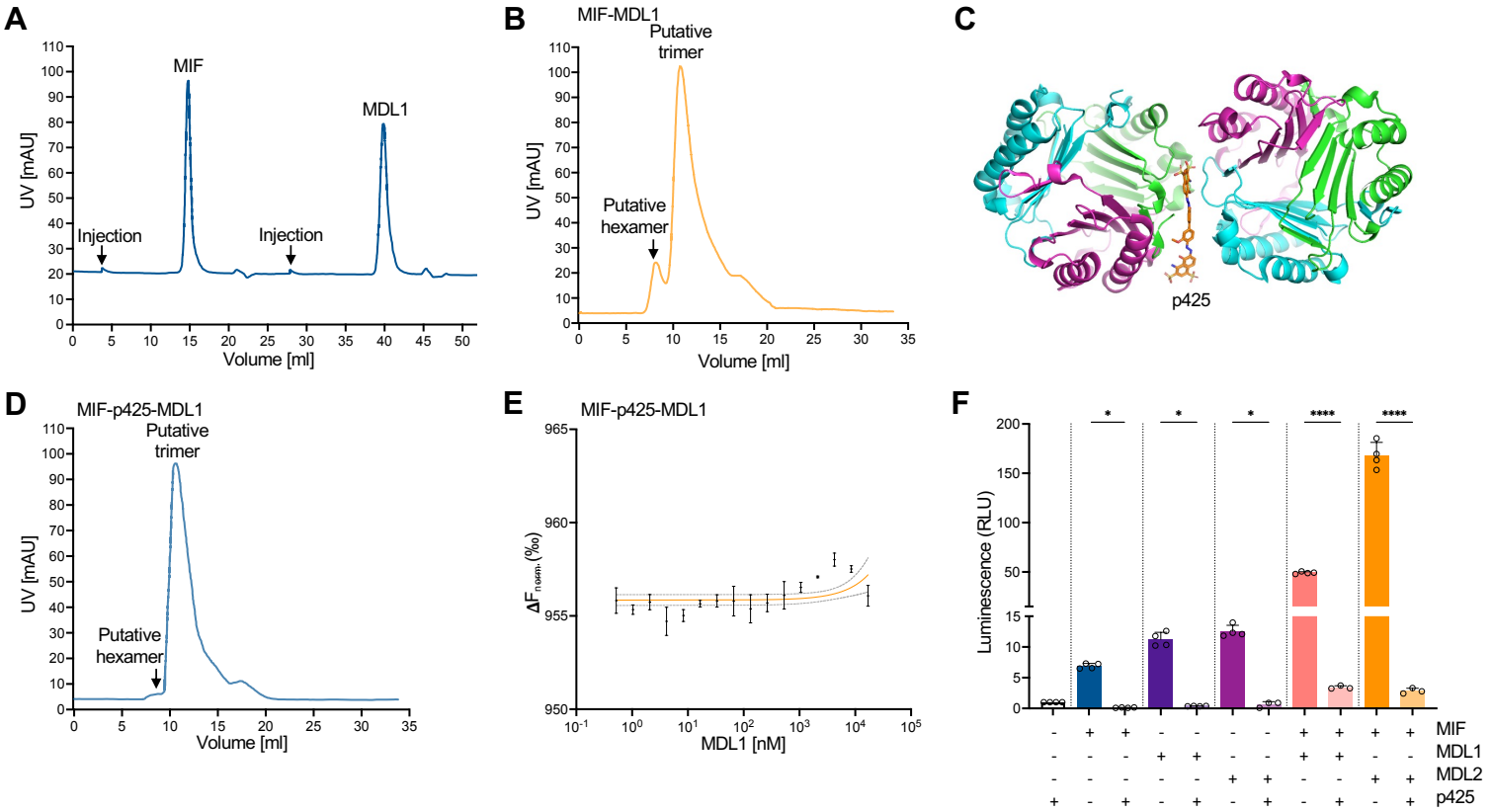
A
MIF
MDL1
Injection
Injection
UV [mAU]
Volume [ml]
B
MIF-MDL1
Putative trimer
Putative hexamer
UV [mAU]
Volume [ml]
C
p425
D
MIF-p425-MDL1
Putative trimer
Putative hexamer
UV [mAU]
Volume [ml]
E
MIF-p425-MDL1
MDL1 [nM]
F
Luminescence (RLU)
MIF
MDL1
MDL2
p425

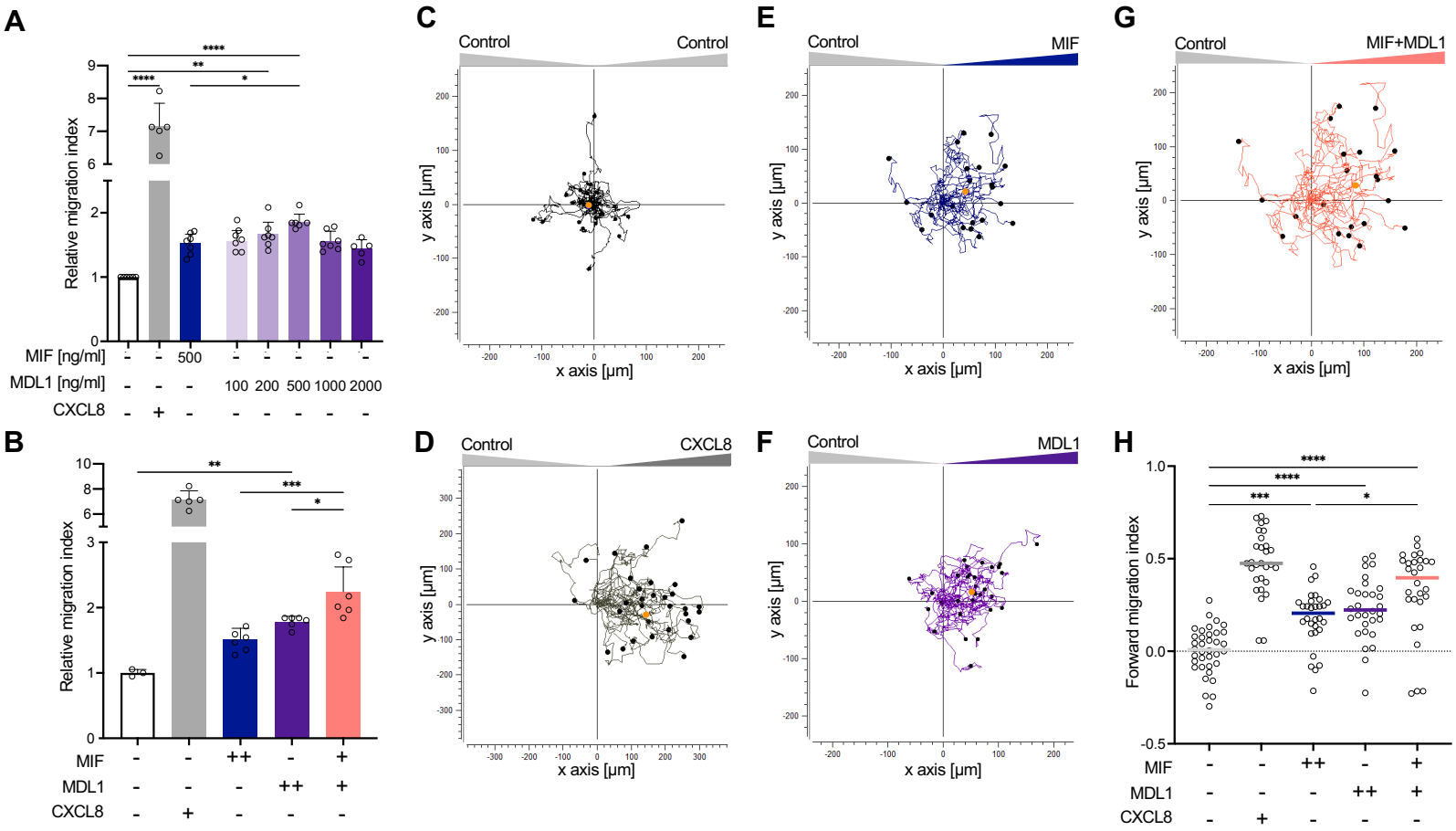
A
Relative migration index
MIF [ng/ml]
MDL1 [ng/ml]
CXCL8
100 200 500 1000 2000
B
Relative migration index
MIF
MDL1
CXCL8
C
Control
Control
y axis [µm]
x axis [µm]
D
Control
CXCL8
E
Control
MIF
F
Control
MDL1
G
Control
MIF+MDL1
H
Forward migration index
MIF
MDL1
CXCL8

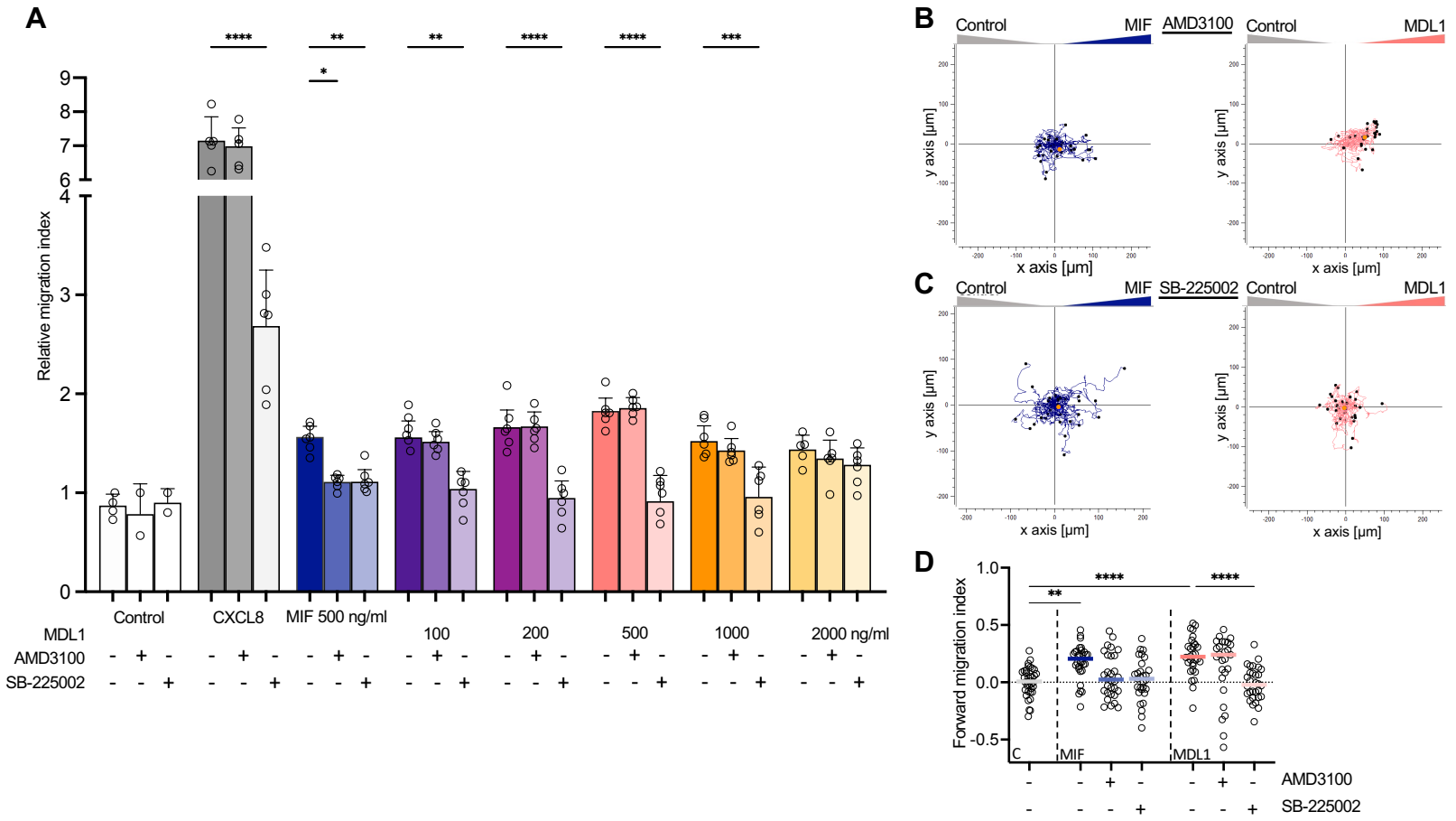
A
B
C
D
Relative migration index
Control
CXCL8
MIF 500 ng/ml
100
200
500
1000
2000 ng/ml
MDL1
AMD3100
SB-225002
Control
MIF
AMD3100
MDL1
SB-225002
y axis [µm]
x axis [µm]
Forward migration index
C
MIF
MDL1

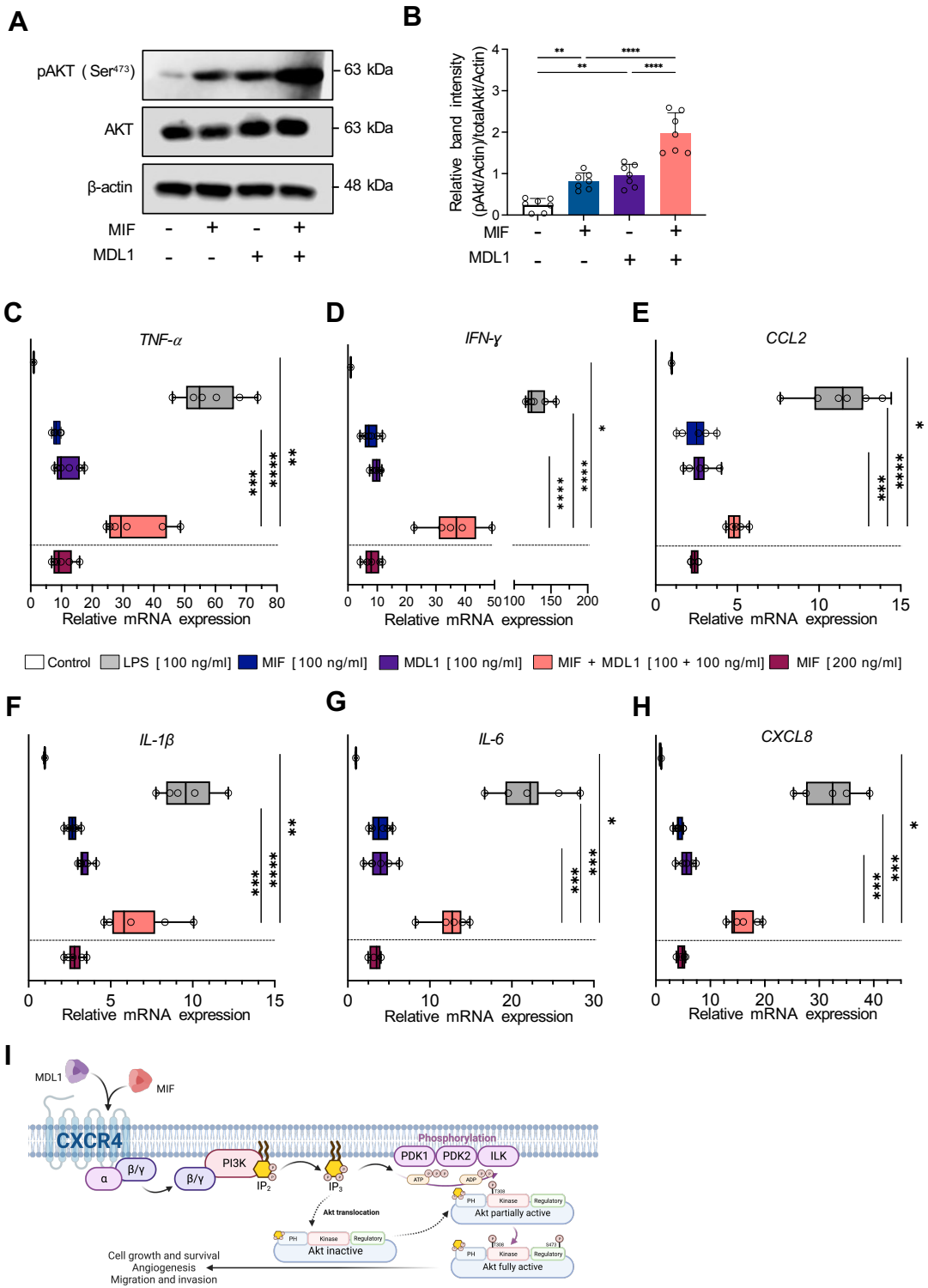
A
pAKT (Ser473)
AKT
β-actin
63 kDa
63 kDa
48 kDa
MIF - + - +
MDL1 - - + +
B
Relative band intensity (pAkt/Actin)/totalAkt/Actin)
MIF - + - +
MDL1 - - + +
C
TNF-α
Relative mRNA expression
D
IFN-γ
Relative mRNA expression
E
CCL2
Relative mRNA expression
Control
LPS [100 ng/ml]
MIF [100 ng/ml]
MDL1 [100 ng/ml]
MIF + MDL1 [100 + 100 ng/ml]
MIF [200 ng/ml]
F
IL-1β
Relative mRNA expression
G
IL-6
Relative mRNA expression
H
CXCL8
Relative mRNA expression
I
MDL1
MIF
CXCR4
α
β/γ
β/γ
PI3K
IP2
IP3
Phosphorylation
PDK1
PDK2
ILK
Akt translocation
Akt partially active
Akt inactive
Akt fully active
Cell growth and survival
Angiogenesis
Migration and invasion

You cannot edit the Supplementary Materials in the galley proofs. See notes at the beginning of the main text Word file. Use the clean Word files downloaded from https://cts.sciencemag.org in your revision. Leave the Track Changes function on. Add a response to each Comment.

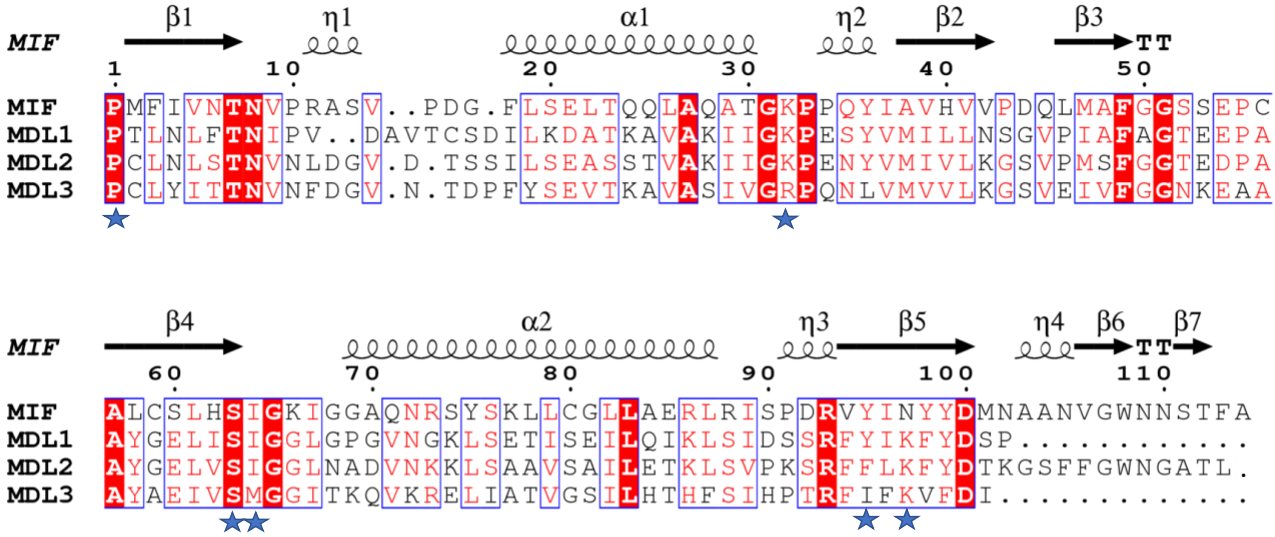

Fig. S1. Structure-based sequence alignment of the *Arabidopsis* MDLs and human MIF. The ESpript application (35) was used to align the structures. The red boxes highlight the invariant residues among the three MDLs and MIF. Similar residues and regions are surrounded by blue boxes. The secondary structure elements are noted above the sequences, with the 3_{10}-helix represented by the η symbol, helices with squiggles, β-strands with arrows, and β-turns with TT letters. Blue stars below the aligned sequences indicate the position of residues in the tautomerase catalytic site of MIF. The last 12 and 9 residues of MDL1 and MDL3, respectively, are not aligned due to the lack of electron density. Some MIF studies refer to the initiating Met^1, which is later posttranslationally cleaved, as the first residue, but in this and some other studies, Pro^1 is used as the first residue. After residue 17, there is one extra amino acid in a loop for all three MDLs relative to MIF, resulting in residue numbers for MDLs that are greater than those for the corresponding residues in MIF.

You cannot edit the Supplementary Materials in the galley proofs. See notes at the beginning of the main text Word file. Use the clean Word files downloaded from https://cts.sciencemag.org in your revision. Leave the Track Changes function on. Add a response to each Comment.

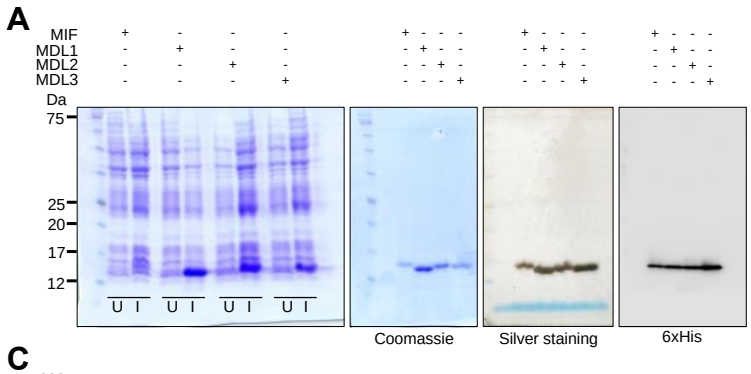

B

Protein	LPS concentration in EU/ml	LPS concentration in ng/ml
MIF-6xHIS	1.36 +/- 0.16	0.136 +/- 0.016
MDL1-6xHIS	1.43 +/- 0.15	0.143 +/- 0.015
MDL2-6xHIS	1.45 +/- 0.23	0.145 +/- 0.023
MDL3-6xHIS	1.38 +/- 0.11	0.138 +/- 0.011

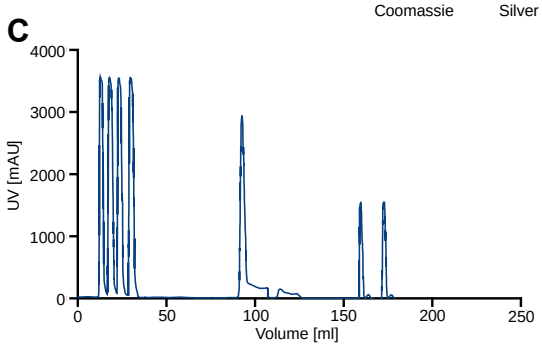

Fig. S2. Expression and purification of recombinant MIF and MDL proteins. (**A**) Electrophoretic analysis of crude protein lysates before (uninduced, [U]) and after induction [I] with isopropyl-β-D-thiogalactopyranoside (IPTG). Cell lysates are shown with Coomassie staining. Purified proteins after immobilized metal affinity chromatography (IMAC) and subsequent size exclusion chromatography (SEC) are also shown using Coomassie staining, silver staining, and immunoblotting with an antibody directed against the hexahistidine tag. The blots shown are representative of at least n = 3 independent experiments. (**B**) Quantification of lipopolysaccharide (LPS) content in purified recombinant proteins using a chromogenic endotoxin detection assay. LPS concentrations are given in endotoxin units (EU)/mL and ng/mL. Values are from three biological replicates (n=3). (**C**) Chromatogram of IMAC and subsequent SEC purification shown for MDL1 as an example. Injections of the bacterial lysate (up to 50 mL) are followed in the course of the elution of the hexahistidine-tagged protein by an imidazole gradient (around 100 mL). For further purification and buffer exchange, this step was followed by two runs of SEC (from 150 mL onward). The chromatogram is representative of at least n = 3 independent experiments.

You cannot edit the Supplementary Materials in the galley proofs. See notes at the beginning of the main text Word file. Use the clean Word files downloaded from https://cts.sciencemag.org in your revision. Leave the Track Changes function on. Add a response to each Comment.

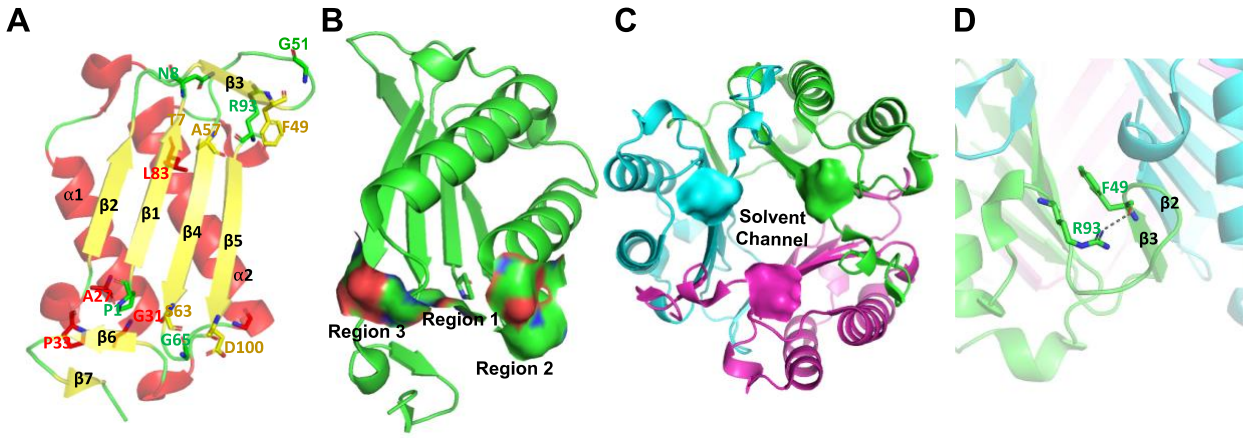

Fig. S3. Structural views and regions of the invariant residues in MIF and MDL proteins. (**A**) All 14 invariant residues among the three MDLs and MIF are shown in a MIF monomer. (**B**) Surface areas of regions 1, 2, and 3. Region 1 contains the Pro^{1} and Ser^{63} of the tautomerase enzymatic site. Region 2 consists of Ala^{27}, Gly^{31}, Pro^{33}, Gly^{65}, Ser^{63}, and Asp^{100}. For Ser^{63}, the backbone atoms are in region 2, whereas the side chain is part of region 1. (**C**) The human MIF trimer creates a solvent channel (water molecules not shown) along the 3-fold axis of the trimeric structure. The solvent channel is surrounded by three surface areas (shown as a smooth surfaces) of Asp^{100} side chains from each subunit (shown in different colors) at one end of the channel, which makes up region 3. (**D**) In region 4, a hydrogen bond between the side chain of Arg^{93} and the backbone of Phe^{49} stabilizes the β-strand important for subunit-subunit interactions (cartoons in blue and green represent two different subunits).

You cannot edit the Supplementary Materials in the galley proofs. See notes at the beginning of the main text Word file. Use the clean Word files downloaded from https://cts.sciencemag.org in your revision. Leave the Track Changes function on. Add a response to each Comment.

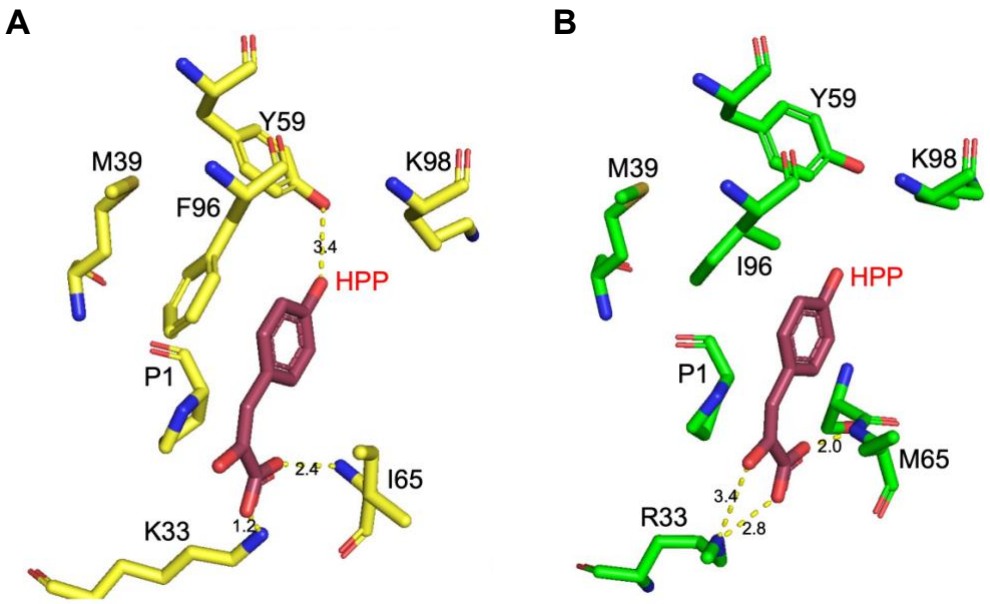

Fig. S4. Interactions of MDL2 and MDL3 tautomerase enzymatic site residues interacting with a modelled HPP substrate molecule. Residues of **(A)** MDL2 and **(B)** MDL3 analogous to the tautomerase catalytic site in human MIF, shown in yellow and green, respectively, were superimposed on the MIF-HPP complex to examine putative interactions between ligand and protein. Potential hydrogen bonds are shown between the MDLs and HPP represented by yellow lines.

You cannot edit the Supplementary Materials in the galley proofs. See notes at the beginning of the main text Word file. Use the clean Word files downloaded from https://cts.sciencemag.org in your revision. Leave the Track Changes function on. Add a response to each Comment.

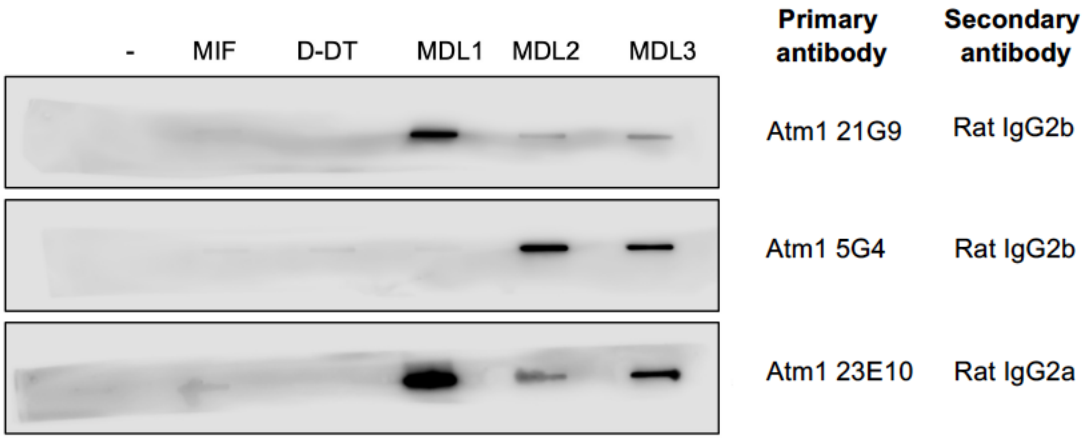

Fig. S5. Slot blot screening for sensitivity and specificity of custom-made monoclonal antibodies directed against MDL1 and MDL2. Custom-made monoclonal antibodies generated against MDL1 and MDL2 were screened by slot blotting. Promising monoclonal antibodies directed against MDL1 and MDL2 were probed against purified recombinant human MIF (MIF), human MIF-2/D-DT, and the three *Arabidopsis* MDL proteins as indicated. The far left-hand lane (-) was a negative control without protein. HRP-coupled immunoglobulin subclass-specific secondary antibodies were used as indicated for detection. Antibody clones directed against MDL2 were previously established (*34*). Clone Atm-5G4, generated against MDL2, was used in this study also recognizes MDL3. Two candidate antibodies directed against MDL1 (Atm1_21G9 and Atm1_23E10) distinguished between MIF or D-DT and the MDLs, but Atm_21G9 showed greater specificity for MDL1. Screening was performed with the primary hybridoma supernatant (shown here) and then validated with the established clone, which was used for subsequent experiments. The blot is representative of n = 3 independent experiments.

You cannot edit the Supplementary Materials in the galley proofs. See notes at the beginning of the main text Word file. Use the clean Word files downloaded from https://cts.sciencemag.org in your revision. Leave the Track Changes function on. Add a response to each Comment.

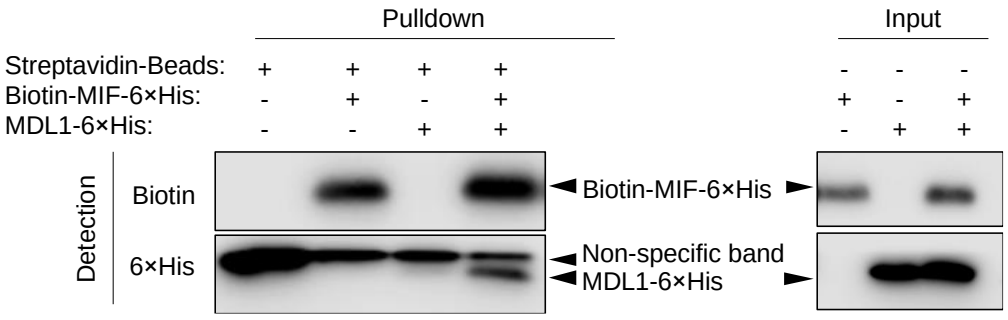

Fig. S6. MIF and MDL proteins bind to each other in vitro. (A) Purified tagged MIF (biotin-MIF-6×His) and MDL1 (MDL1-6×His) were incubated alone or together, and complexes pulled down by streptavidin-coated beads were immunoblotted after separation by SDS-PAGE. Blots were developed for His-tagged proteins by using a hexahistidine tag–specific antibody to visualize MIF and MDL1. The upper band in the bottom panel of the pulldown, absent in the input samples, originates from the streptavidin-coated beads used to pull down biotin-tagged MIF and is non-specific. Blots are representative of n = 3 independent experiments.

You cannot edit the Supplementary Materials in the galley proofs. See notes at the beginning of the main text Word file. Use the clean Word files downloaded from https://cts.sciencemag.org in your revision. Leave the Track Changes function on. Add a response to each Comment.

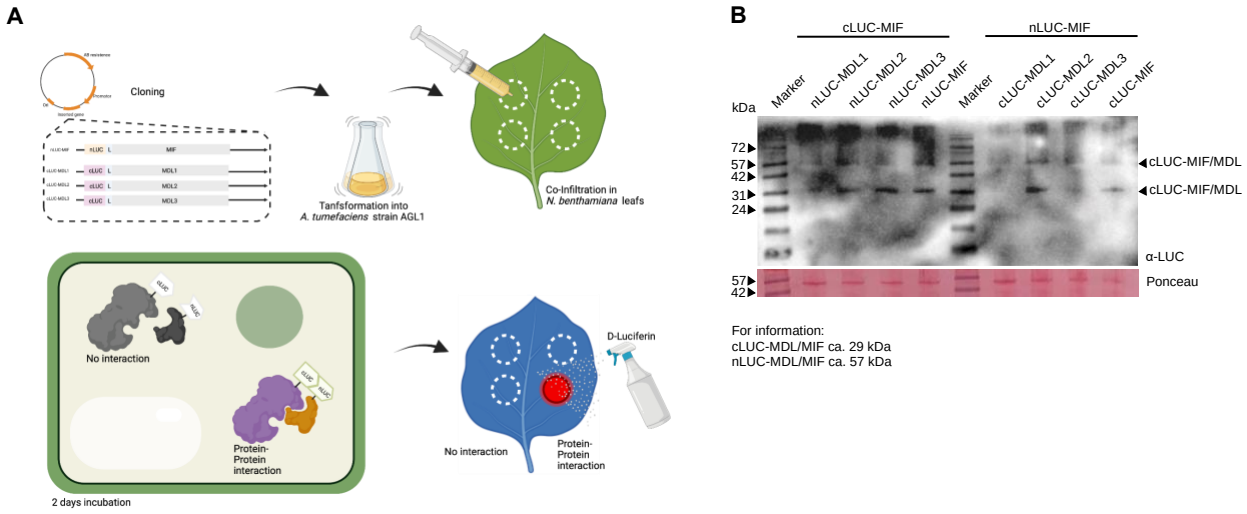

Fig. S7. Luciferase complementation imaging assay. (**A**) Schematic illustration of luciferase complementation imaging assay upon transient expression of test genes in *N. benthamiana* leaves. Constructs of *MIF* and three *MDL* genes were N-terminally fused to N- and C-terminal segments of firefly luciferase. These plasmids were transferred into *A. tumefaciens* strain GV3101 (pmP90RK) for subsequent transformation into plant cells. For co-infiltration, equal volumes of each *A. tumefaciens* transformant culture were mixed and infiltrated with a syringe lacking a cannula from the lower (abaxial) side into fully expanded leaves of four- to six-week-old *N. benthamiana* plants. Imaging was done after three days of incubation following spraying the leaves with the lucifase substrate D-luciferin. (**B**) Immunoblot analysis of transient expression of luciferase complementation fusion proteins. Protein extracts of *A. tumefaciens* infiltrated *N. benthamiana* leaves were separated by SDS-PAGE, blotted onto a nitrocellulose membrane, and probed with a luciferase-specific primary antibody and a secondary antibody coupled to horseradish peroxidase (HRP). Chemiluminescence detection of antigen-antibody complexes was performed with SuperSignal™ West Femto Western substrate. As a loading control, membranes were stained in Ponceau S solution, showing primarily the large subunit of ribulose-1,5-bisphophate carboxylase/oxygenase, a prominent protein of ~56 kDa in plant protein extracts. Expected molecular masses are ~57 kDa for the nLUC-MIF/MDL fusion proteins and ~29 kDa for the cLUC-MIF/MDL fusion proteins. Three independent luciferase complementation imaging assays were performed. The blot shown was performed from one of these experiments. X

You cannot edit the Supplementary Materials in the galley proofs. See notes at the beginning of the main text Word file. Use the clean Word files downloaded from https://cts.sciencemag.org in your revision. Leave the Track Changes function on. Add a response to each Comment.

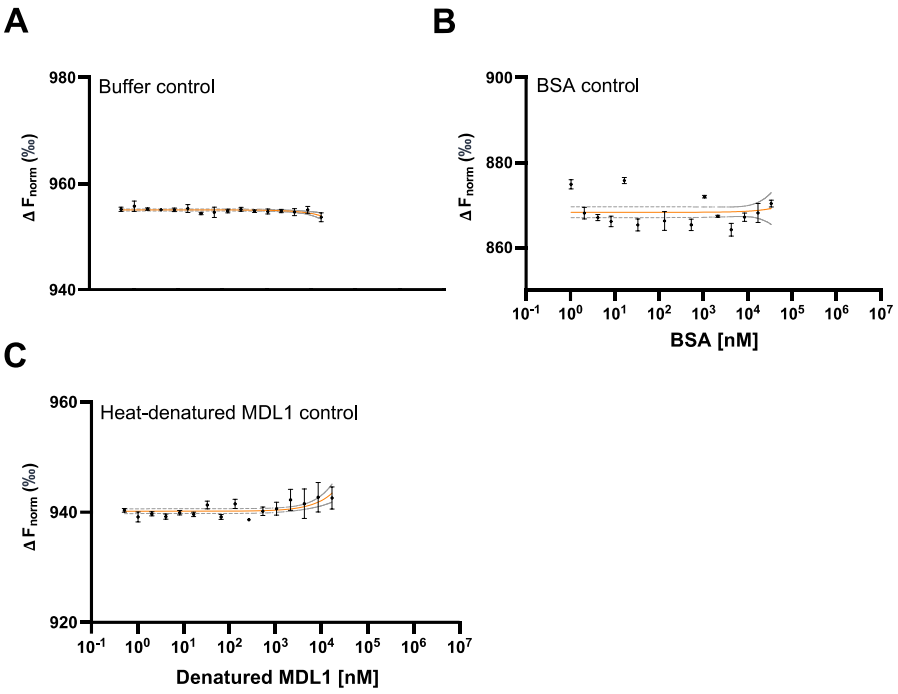

Fig. S8. Microscale thermophoresis (MST) control experiments. RED-NHS-MIF was tested in MST in different control conditions: (**A**) buffer control**,** (**B**) bovine serum albumin (BSA) as an unrelated control protein instead of MDL, and (**C**) heat-denatured MDL1 as a negative control for folded MDL1 protein. Settings and buffer conditions were the same as for the MIF-MDL experiments (20 mM sodium phosphate buffer, pH 7.2, containing 0.2% Tween-20). Values shown represent means ± SD as obtained from at least 3 biological replicates (n≥3). Data analysis and K_D-fitting was performed using NanoTemper MOcontrol software, visualization was done by non-linear fitting using Graphpad Prism.

You cannot edit the Supplementary Materials in the galley proofs. See notes at the beginning of the main text Word file. Use the clean Word files downloaded from https://cts.sciencemag.org in your revision. Leave the Track Changes function on. Add a response to each Comment.

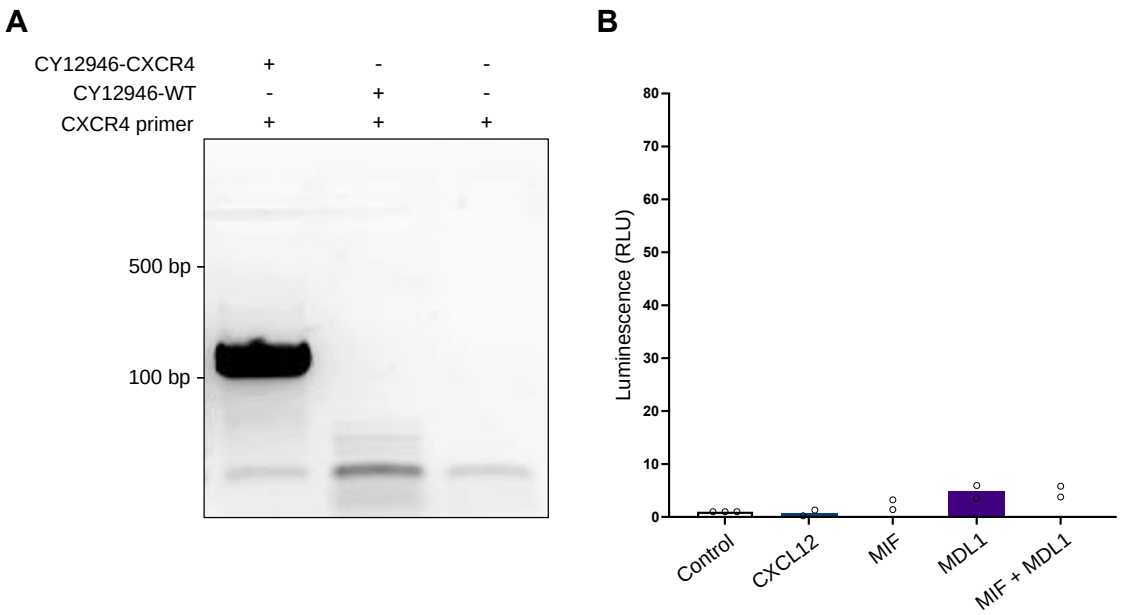

Fig. S9. A plasmid loss assay confirms the specificity of MIF and MDL effects in the yeast-based reporter system. The plasmid loss assay for the CXCR4-encoding plasmid was carried out as described in the Materials and Methods. (**A**) PCR confirms loss of the CXCR4-encoding plasmid from the yeast hCXCR4 clone (CY12946-CXCR4). The new clone lacking CXCR4 is designated CY12946-WT. (**B**) Control experiment with clone CY12946-WT, generated according to (A). Thirty minutes after addition of test proteins to the yeast system, luminescence (in relative light units, RLU) due to *lacZ* reporter gene activation was measured. MIF and MDL1 were used individually at 20 µM or in combination (10 µM each). Only minimal unspecific activation of the lacZ reporter pathway was observed in the yeast cells that have lost the CXCR4-encoding plasmid, confirming the specificity of the effects measured in the CXCR4 yeast reporter system. The effect with the cognate CXCR4 ligand CXCL12 (tested at 2 µM) is shown for comparison. Values shown represent means as obtained from two independent experiments (n=2), with RLUs of each experiment assessed in technical duplicates and normalized to untreated controls. Individual data points are indicated by white circles.

You cannot edit the Supplementary Materials in the galley proofs. See notes at the beginning of the main text Word file. Use the clean Word files downloaded from https://cts.sciencemag.org in your revision. Leave the Track Changes function on. Add a response to each Comment.

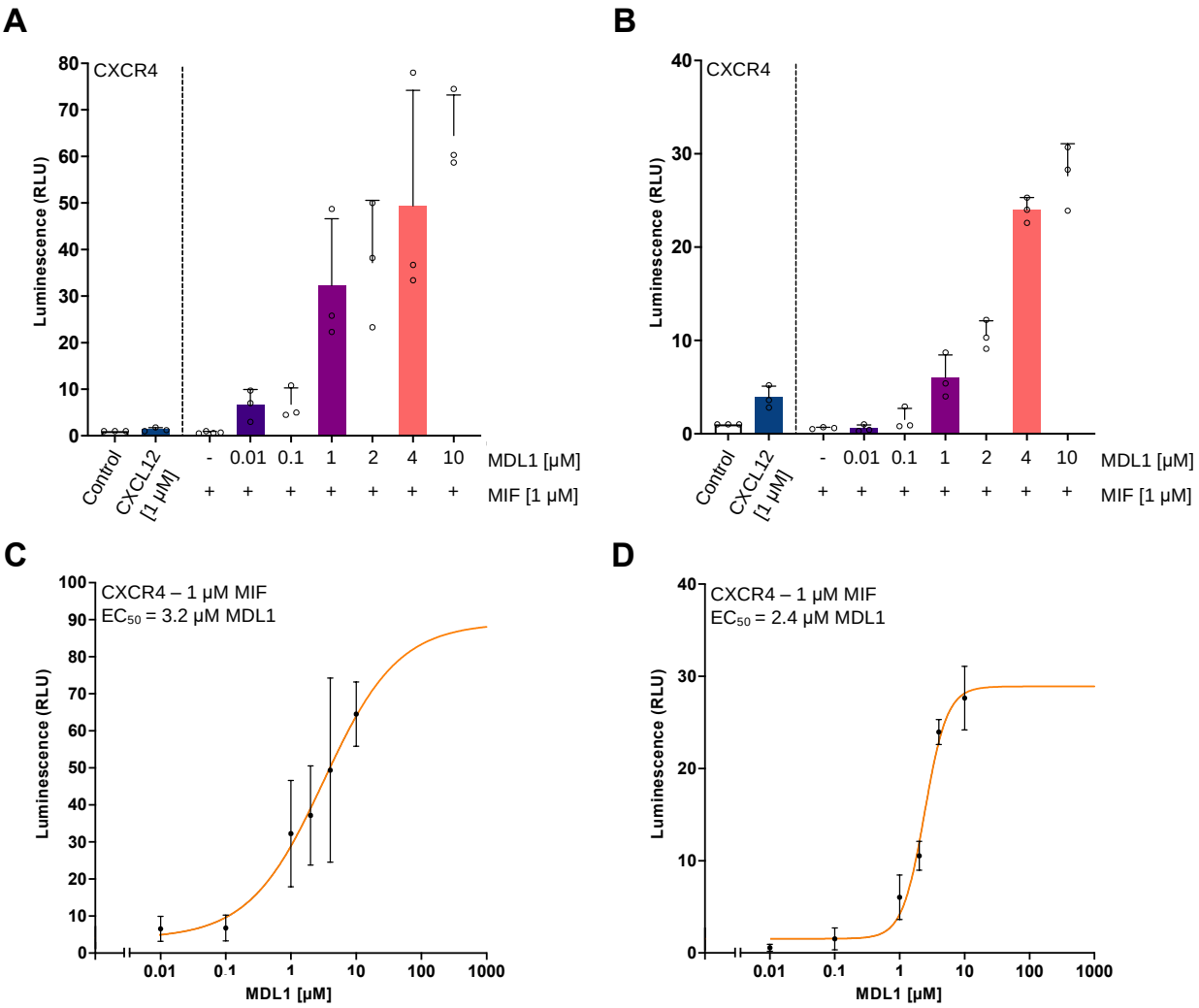

You cannot edit the Supplementary Materials in the galley proofs. See notes at the beginning of the main text Word file. Use the clean Word files downloaded from https://cts.sciencemag.org in your revision. Leave the Track Changes function on. Add a response to each Comment.

Fig. S10. Additional biological replicates showing synergistic CXCR4 activation by MIF and MDL1 in the yeast-based reporter system. Shown are two additional biological replicates of the concentration-response experiments (Fig. 3, H and I). (**A and B**) The bar diagrams show luminescence (in RLU) due to *lacZ* reporter gene activation upon the addition of a sub-threshold concentration of 1 µM MIF and increasing concentrations (0 - 10 µM) of MDL1. The effect of the cognate CXCR4 ligand CXCL12 (at 1 µM) is shown for comparison. (**C and D**) Concentration-response curves for MIF-MDL1 interaction in the CXCR4 reporter system according to (A) and (B), respectively, assuming a non-linear fit. From those fits, a half-maximal effective ('synergistic') concentration (EC_{50}) of 3.2 and 2.4 µM MDL1, respectively, was derived. Each experiment was carried out in technical triplicates. White circles indicate individual data points.

You cannot edit the Supplementary Materials in the galley proofs. See notes at the beginning of the main text Word file. Use the clean Word files downloaded from https://cts.sciencemag.org in your revision. Leave the Track Changes function on. Add a response to each Comment.

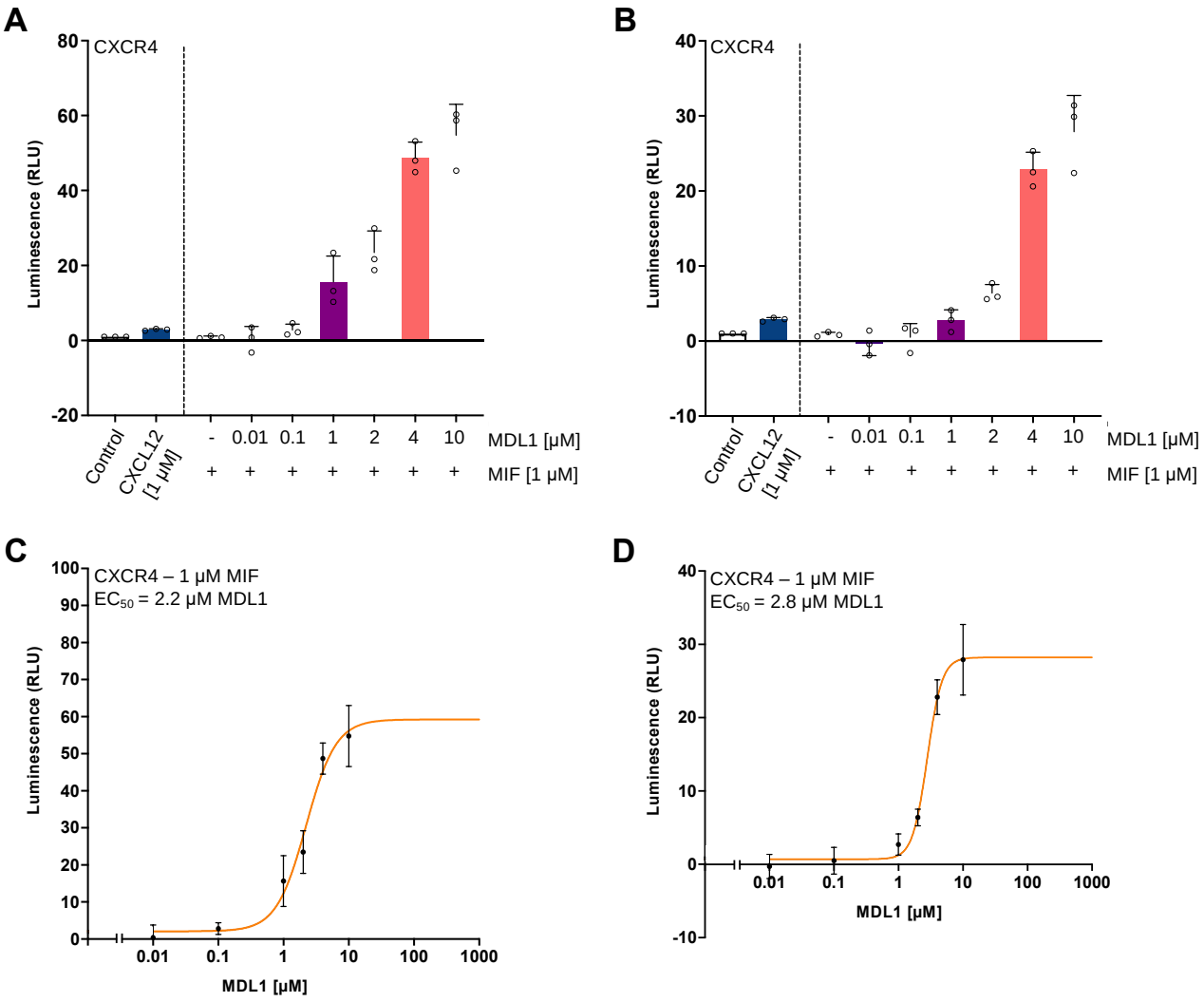

You cannot edit the Supplementary Materials in the galley proofs. See notes at the beginning of the main text Word file. Use the clean Word files downloaded from https://cts.sciencemag.org in your revision. Leave the Track Changes function on. Add a response to each Comment.

Fig. S11. Subtraction of the effect of MDL1 alone from experiments showing synergistic CXCR4 activation by MIF and MDL1 in the yeast-based reporter system. Shown are two biological replicates of the concentration-response experiment with combinations of constant MIF and increasing MDL1 concentrations (fig. S10, A to D), with the respective MDL1-alone values subtracted. (**A and B**) Bar diagrams show luminescence (RLU) due to *lacZ* reporter gene activation upon addition of a sub-threshold concentration of 1 µM MIF and increasing concentrations (0 - 10 µM) of MDL1. Luminescence of MDL1-alone at 0.01, 0.1, 1, 2, 4, 10 µM (measured separately) was deducted from values observed for the respective MIF + MDL1 combinations. Negative RLU values for combinations of MIF and low MDL1 concentration are due to this subtraction. The effect of the cognate CXCR4 ligand CXCL12 (at 1 µM) is shown for comparison. (**C and D**) Concentration-response curves for MIF-MDL1 interaction in the CXCR4 reporter system according to (A) and (B), respectively, assuming a non-linear fit. From those fits, a half-maximal effective ('synergistic') concentration (EC_{50}) of 2.2 and 2.8 µM MDL1, respectively, was derived. Each experiment was carried out in technical triplicates. White circles indicate individual data points.

You cannot edit the Supplementary Materials in the galley proofs. See notes at the beginning of the main text Word file. Use the clean Word files downloaded from https://cts.sciencemag.org in your revision. Leave the Track Changes function on. Add a response to each Comment.

A

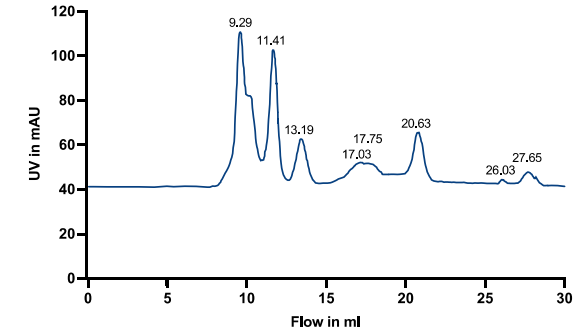

B

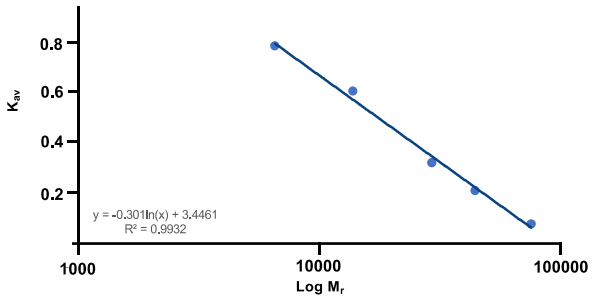

C

$$Mr = e^{\frac{\left(\frac{V_e - V_0}{V_c - V_0}\right) - 3.4461}{-0.301}}$$

D

Calibration probe	Actual Mr [Da]	Calculated Mr [Da]
Conalbumin	75000	72582
Ovalbumin	44000	46659
Carbonic anhydrase	29000	32196
RNase A	13700	12447
Aprotinin	6500	6830

Fig. S12. Establishing a calibration curve and a standard equation for the Superdex 75 10/300 SEC column. The GE Healthcare Gel Filtration Calibration Kit was used to establish a standard curve and equation for the following conditions: 20 mM sodium phosphate buffer including 20 mM sodium chloride, pH 7.2, flow rate 0.5 mL/min. (**A**) Standard proteins with known molecular masses were prepared, mixed according to manufacturer's instructions and run over the column under the aforementioned conditions. The chromatogram shows the elution profile of the standard proteins with their corresponding elution volumes. (**B**) Standard curve generated from the known molecular mass and the observed elution volume for each of the test proteins. Notice the logarithmic x-axis. (**C**) Standard equation to calculate the molecular mass (Mr) of a protein according to its elution volume **(V_e).** V_0 = column volume, e = Euler's number. (**D**) Comparison of the known molecular masses of test proteins to their calculated mass based on their elution volumes (V_e) and the standard equation shown in (C).

You cannot edit the Supplementary Materials in the galley proofs. See notes at the beginning of the main text Word file. Use the clean Word files downloaded from https://cts.sciencemag.org in your revision. Leave the Track Changes function on. Add a response to each Comment.

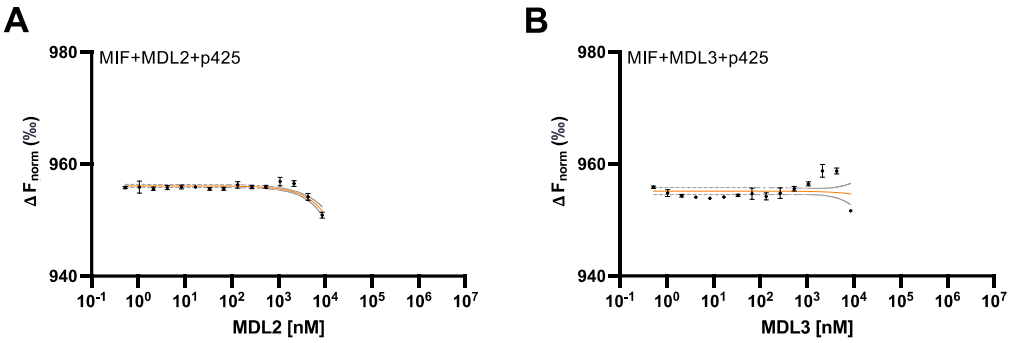

Fig. S13. p425 blocks the interaction between MIF and MDL2 or MDL3. The interaction between RED-NHS-MIF and different concentrations of (**A**) MDL2 or (**B**) MDL3 in the presence of the MIF allosteric inhibitor p425 was determined by microscale thermophoresis (MST). Values shown represent means ± SD as obtained from at least 3 biological replicates (n≥3). Data analysis and K_D-fitting was performed using NanoTemper MOcontrol software, visualization was done by non-linear fitting using Graphpad Prism.

You cannot edit the Supplementary Materials in the galley proofs. See notes at the beginning of the main text Word file. Use the clean Word files downloaded from https://cts.sciencemag.org in your revision. Leave the Track Changes function on. Add a response to each Comment.

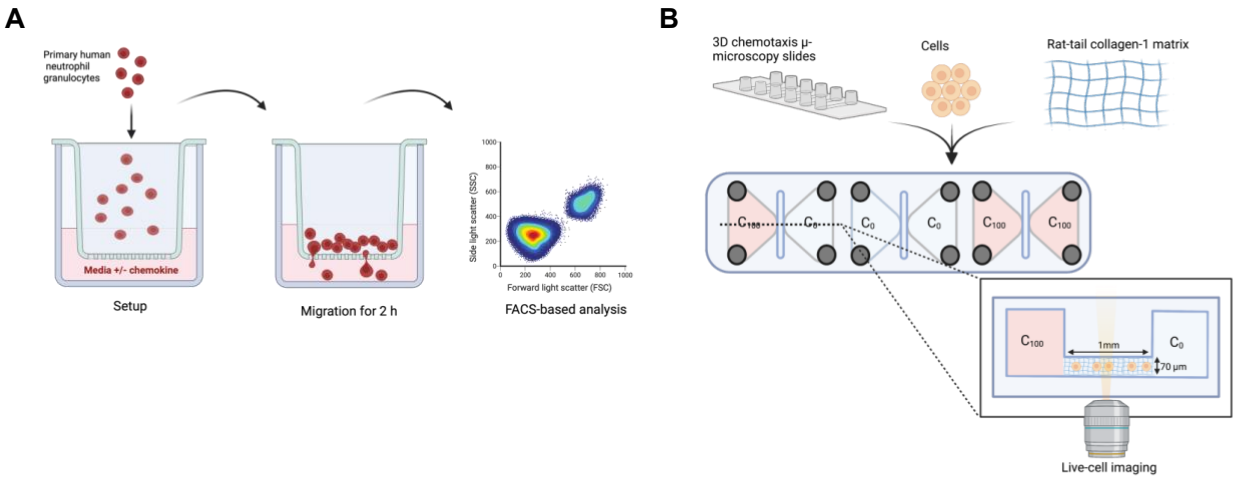

Fig. S14. Schematic illustrations of experiments used to study the chemotactic movement of primary human neutrophils. (**A**) Schematic illustration of the Transwell migration assay. Neutrophils migrating across the filter towards a chemotactic stimulus were quantified by flow cytometry. (**B**) Schematic illustration of the 3D collagen matrix migration assay using time-lapse live-cell microscopy and individual cell tracking, using the 3D-chemotaxis µ-Slide system from Ibidi GmbH. Migration along this gradient was observed using time-lapse imaging for 1 h at 37 °C on a Leica inverted DMi8-Life Cell Imaging system.

You cannot edit the Supplementary Materials in the galley proofs. See notes at the beginning of the main text Word file. Use the clean Word files downloaded from https://cts.sciencemag.org in your revision. Leave the Track Changes function on. Add a response to each Comment.

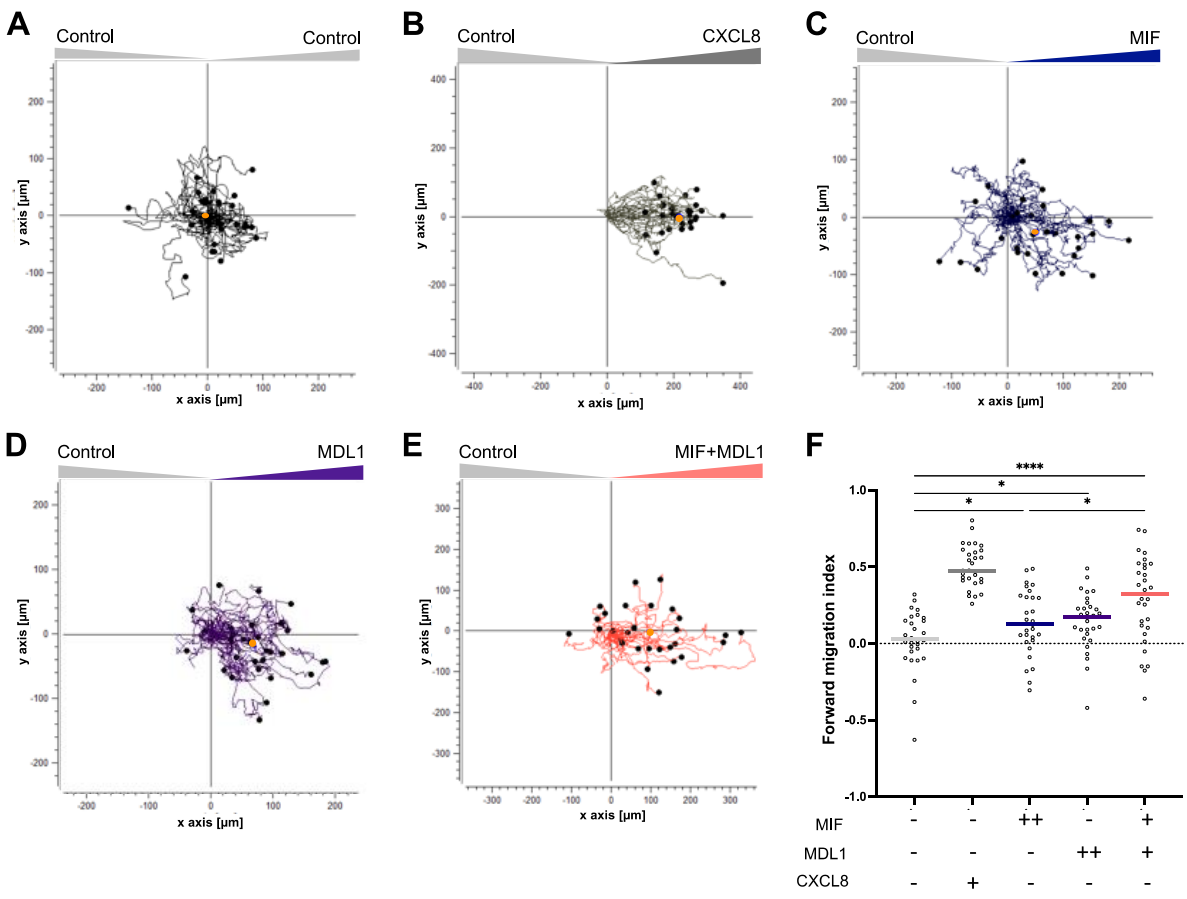

You cannot edit the Supplementary Materials in the galley proofs. See notes at the beginning of the main text Word file. Use the clean Word files downloaded from https://cts.sciencemag.org in your revision. Leave the Track Changes function on. Add a response to each Comment.

Fig. S15. MDLs promote human neutrophil chemotaxis and augment the chemotactic effect of human MIF. Chemotaxis was assessed by 3D chemotaxis of primary human neutrophils applying live-cell microscopy of single-cell migration tracks in x/y direction in µm. **(A to E**) Representative experiments showing 3D chemotaxis of primary human neutrophils towards (**A**) buffer control (gray), indicating random motility; (**B**) CXCL8 (1 µM); (**C**) MIF (500 ng/mL); (**D**) MDL1 (500 ng/mL); or (**E**) a 1:1 mixture of MIF and MDL1 (250 ng/mL each). Orange dots represent the center of mass in each experiment. (**F**) Quantification of (A to E). The migration tracks of 30 randomly selected cells per treatment group (n=30) were recorded and the forward migration index plotted. This is an independent biological replication of the experiment shown in the main text (Fig. 5, C to H). Statistical analysis was performed using one-way ANOVA with Tukey's posthoc multiple comparison between the buffer control and the treatment groups (* $p < 0.05$, **** $p < 0.0001$).

You cannot edit the Supplementary Materials in the galley proofs. See notes at the beginning of the main text Word file. Use the clean Word files downloaded from https://cts.sciencemag.org in your revision. Leave the Track Changes function on. Add a response to each Comment.

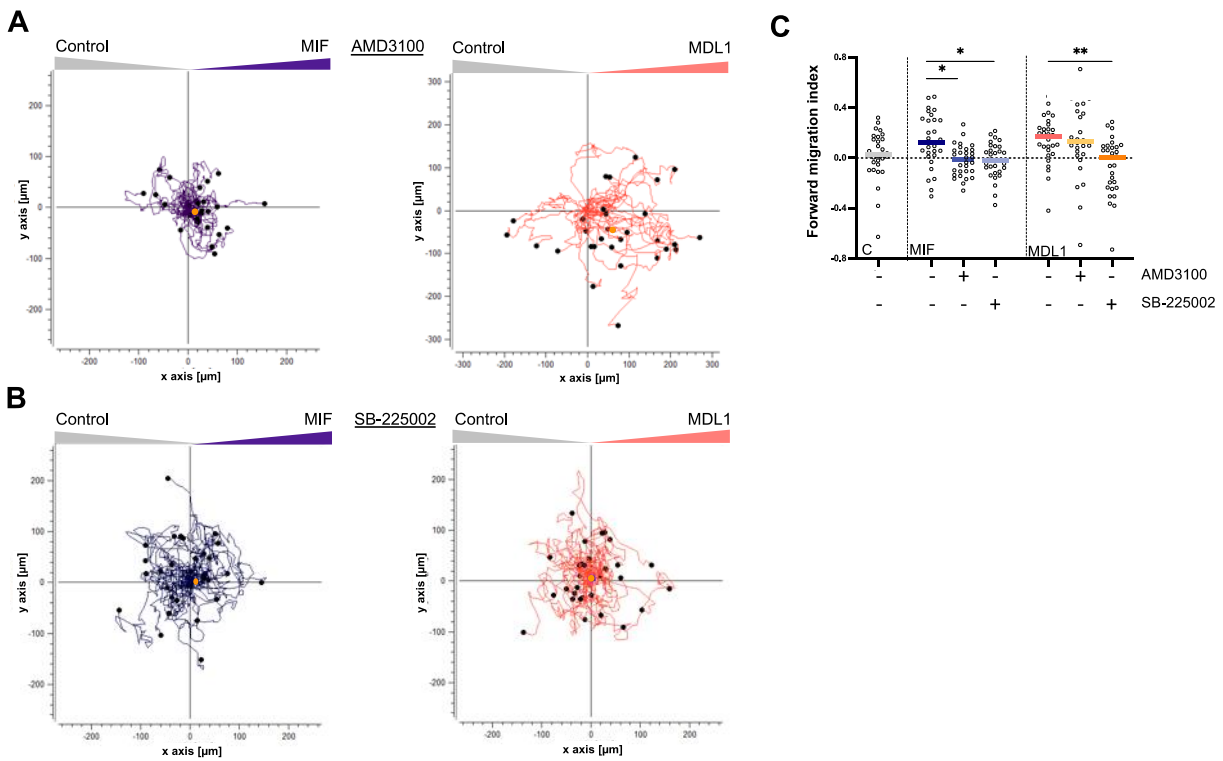

Fig. S16. MDL1-mediated neutrophil chemotaxis is inhibited by SB-225002 but not by AMD3100. 3D chemotaxis of primary human neutrophils as assessed by live-cell microscopy of single-cell migration tracks in x/y direction in µm. (**A and B**) Representative experiments showing 3D chemotaxis of primary human neutrophils. Shown is the comparison between migration towards MIF (500 ng/mL) or MDL1 (500 ng/mL) in the presence of either the CXCR4 I nhibitor AMD3100 (A); or the CXCR2 inhibitor SB225002 (B). Orange dots represent the center of mass for each experiment. (**C**) Quantification of (B) and (C) plus experiments performed in the absence of the inhibitors. The migration tracks of 30 randomly selected cells per treatment group were recorded and the forward migration index plotted. This is an independent biological replication of this experiment is shown in the main text (Fig. 6, B to D). Statistics were performed using one-way ANOVA with Tukey's posthoc multiple comparison (* $p < 0.05$, ** $p < 0.01$).

You cannot edit the Supplementary Materials in the galley proofs. See notes at the beginning of the main text Word file. Use the clean Word files downloaded from https://cts.sciencemag.org in your revision. Leave the Track Changes function on. Add a response to each Comment.

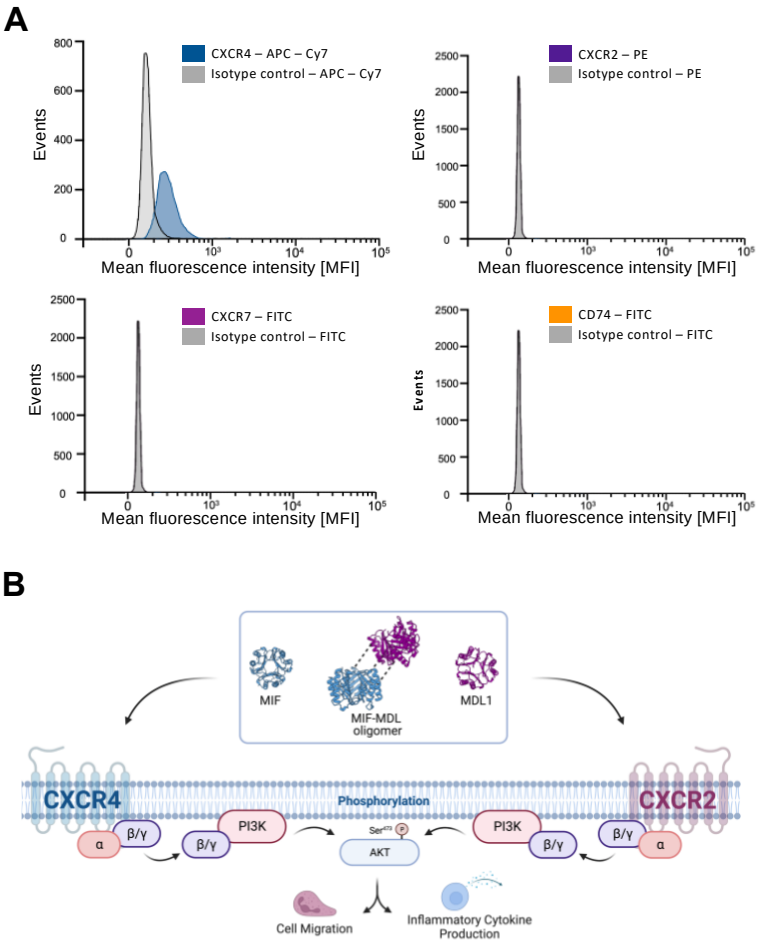

Fig. S17. MIF receptor expression in A549 lung epithelial cells and the CXCR4-PI3K-AKT signaling pathway. (A) Surface CXCR4 on A549 lung epithelial cells as assessed by flow cytometry. The histogram represents the mean fluorescence intensity (MFI) on the x-axis and the number of fluorescent events on the y-axis. Antibody staining for CXCR4 (APC-Cy7), CXCR2 (PE), CXCR7 (FITC), CD74 (FITC) as well as staining with the corresponding isotype control (IgG control, grey) are shown. Data are representative of n = 3 independent experiments. (**B**) Schematic illustration of the CXCR4 receptor (a typical GPCR) and PI3K (phosphoinositid-3-kinase) as well as the AKT pathway as one of its downstream signaling cascades known to be involved in cell proliferation and migration. MIF or MDL1 binding to CXCR4 results in activation of the pathway as indicated.

You cannot edit the Supplementary Materials in the galley proofs. See notes at the beginning of the main text Word file. Use the clean Word files downloaded from https://cts.sciencemag.org in your revision. Leave the Track Changes function on. Add a response to each Comment.

Table S1. Crystallographic data and refinement statistics.

Protein (PDB code)	MDL1 (8DQA)	MDL2 (8AP3)	MDL3 (8DQ6)
Wavelength (Å)	0.9999	0.9999	0.9999
Resolution range (Å)	43.53-1.56 (1.616-1.56)	37.32 -1.40 (1.45-1.40)	44.75 -2.0 (2.072- 2.00)
Space group	P 65	P 21 21 21	I 2 3
Unit cell dimensions (Å)	a, b=66.737,c=132.32 α=β=90° γ=120°	a=46.218 b=79.243 c=84.6 α=β=γ=90°	a, b, c=89.499 α=β=γ=90°
Total reflections	931420 (75211)	783989 (72179)	105554 (9776)
Unique reflections	46283 (4257)	61915 (6095)	8229 (804)
Multiplicity	20.1 (17.7)	12.7 (11.8)	12.8 (12.2)
Completeness (%)	97.54 (90.40)	99.96 (100.00)	99.96 (100.00)
Mean I/sigma(I)	31.45 (2.24)	31.44 (3.01)	35.38 (4.35)
Wilson B-factor	26.64	19.22	40.22
R-merge	0.05281 (0.99)	0.04017 (0.6908)	0.04159 (0.5394)
R-meas	0.05418 (1.019)	0.04189 (0.7219)	0.04334 (0.5634)
R-pim	0.012 (0.236)	0.01172 (0.2084)	0.01205 (0.1612)
CC1/2	1 (0.817)	1 (0.907)	1 (0.923)
CC*	1 (0.948)	1 (0.975)	1 (0.98)
Reflections used in refinement	46163 (4256)	61898 (6095)	8227 (804)
Reflections used for R-free	2308 (213)	3173 (272)	375 (37)
R-work	0.1830 (0.2623)	0.1847 (0.2678)	0.2011 (0.2910)
R-free	0.2083 (0.2874)	0.2080 (0.3109)	0.2324 (0.2579)
CC(work)	0.967 (0.842)	0.960 (0.864)	0.957 (0.774)
CC(free)	0.957 (0.815)	0.949 (0.852)	0.906 (0.927)
Number of non-hydrogen atoms	2437	2823	784
macromolecules	2297	2602	752
solvent	134	221	32
Protein residues	309	351	100
RMS(bonds)	0.006	0.009	0.002
RMS (angles)	0.84	1.09	0.49
Ramachandran favored (%)	100.00	97.97	97.96
Ramachandran allowed (%)	0.00	2.03	2.04
Ramachandran outliers (%)	0.00	0.00	0.00

You cannot edit the Supplementary Materials in the galley proofs. See notes at the beginning of the main text Word file. Use the clean Word files downloaded from https://cts.sciencemag.org in your revision. Leave the Track Changes function on. Add a response to each Comment.

Rotamer outliers (%)	0.40	0.00	0.00
Clashscore	2.60	1.15	1.33
Average B-factor (Å²)	31.29	21.14	44.98
Macromolecules	30.68	20.25	44.93
Solvent	40.57	31.51	46.15

Statistics for the highest-resolution shell are shown in parentheses.

You cannot edit the Supplementary Materials in the galley proofs. See notes at the beginning of the main text Word file. Use the clean Word files downloaded from https://cts.sciencemag.org in your revision. Leave the Track Changes function on. Add a response to each Comment.

Table S2. Primer sequences used for RT-qPCR of proinflammatory genes in A549 cells.

Gene	Forward primer	Reverse primer
TNF-α	CTCTTCTGCCTGCTGCACTTTG	ATGGGCTACAGGCTTGTCACTC
INF-γ	GAGTGTGGAGACCATCAAGGAAG	TGCTTTGCGTTGGACATTCAAGTC
CCL2	AGAATCACCAGCAGCAAGTGTCC	TCCTGAACCCACTTCTGCTTGG
IL-1β	CCACAGACCTTCCAGGAGAATG	GTGCAGTTCAGTGATCGTACAGG
IL-6	AGACAGCCACTCACCTCTTCAG	TTCTGCCAGTGCCTCTTTGCTG
CXCL8	GAGAGTGATTGAGAGTGGACCAC	CACAACCCTCTGCACCCAGTTT
RPLP0	TGGTCATCCAGCAGGTGTTCGA	ACAGACACTGGCAACATTGCGG